Stochastic smoothed profile method for modeling random roughness in flow problems

Mohsen Zayernouri [a], Sang-Woo Park [b], Daniel M. Tartakovsky [b], George Em Karniadakis [a,*]

[a] Division of Applied Mathematics, Brown University, George 182, Providence, RI 02912, USA
[b] Department of Mechanical and Aerospace Engineering, University of California, San Diego, 9500 Gilman Drive, La Jolla, CA 92093, USA

ARTICLE INFO

ABSTRACT

We present an efficient computational method to model fluid flow in the presence of random wall roughness. A random flow domain is represented by a stochastic indicator function having a smoothed profile perpendicular to roughness, and the random domain is discretized with a fixed non-conformal grid. This procedure introduces a stochastic force into the Navier–Stokes equations, and modifies the boundary conditions at the fluid–solid interface. We employ a high-order semi-implicit splitting scheme implemented in the context of a spectral/hp element method in order to discretize the physical domain. The stochastic roughness is treated as a second-order autoregressive process that is represented by a Karhunen–Loève expansion. A multi-element probabilistic collocation method is employed to solve the resulting stochastic Navier–Stokes equations. This method is applied to simulate external flow past a rough cylinder and internal Stokes flow between two parallel plates with random wall roughness. In the first problem, we develop an analytical solution for the asymptotic behavior of the lift coefficient C_L to verify the results. In the second test-case, we compare the mean and the standard deviation of the velocity field to those obtained from a different method called stochastic mapping approach (SMA), developed by Tartakovsky and Xiu (2006).

1. Introduction

Topological uncertainties associated with rough surfaces are of great scientific and engineering importance. Petroleum geology [1], hydraulic network design [2], surface imaging [3], nano-device manufacturing [4], biological wetting mechanisms [5], and human physiology [6] are but a few applications in which (uncertain) boundary roughness significantly affects the physical phenomenon involved. This uncertainty arrises from data scarcity and/or excessive measurement errors. It is ubiquitous not only in natural systems (e.g., geological materials) but also in manufactured ones where imperfect manufacturing, mechanical and electro-chemical corrosion, etc., introduce uncertainty into the representation of surfaces bounding computational domains.

Approaches to quantification of the effects of geometric irregularities on a system's behavior fall into either deterministic or probabilistic frameworks. Deterministic approaches represent surface roughness through canonical shapes, such as indentations, sinusoidal corrugations, periodic segments, or fractals [7–10]. The probabilistic framework conceptualizes rough surfaces as a source of uncertainty and treats them as random fields [11–13].

Consequently, it models even a deterministic physical system as a stochastic boundary-value problem.

The probabilistic framework necessitates the development of new approaches for analysis and solution of partial-differential equations (PDEs) defined on uncertain (random) domains. This is because traditional methods for uncertainty quantification in such problems, including Monte Carlo simulations, can become computationally prohibitive [14]. Examples of analyses focusing on uncertain domains are perturbation solutions of Laplace's equation in a domain bounded by a random fractal surface [10], quantification of the effects of uncertain geometry on solutions of elliptic boundary-value problems [15,16]. Other examples are prediction of geometric uncertainty effects on the dynamics of fluid employing polynomial chaos and the notion of fictitious domain, where the governing PDEs are solved on a domain different from the physical one [17], and implementation of Karhunen-Loève expansion for describing the variability in the nozzle geometry [18].

A general approach for solving PDEs on domains bounded by fixed or moving random surfaces [19] was used to solve a number of problems of practical importance [12,13,20,6]. The approach relies on a stochastic mapping of random domain onto a deterministic domain, which transforms an original (deterministic or stochastic PDE) into a stochastic PDE. When analytical mappings are not available, this method bears an additional computational

* Corresponding author. Tel.: +1 401 863 1217; fax: +1 401 863 2722.
  E-mail address: george_karniadakis@brown.edu (G.E. Karniadakis).

cost associated with solving a set of Laplace's equations to obtain the stochastic mappings.

Here, we present a *stochastic smoothed profile method* (SSPM) as an efficient computational alternative to the latter approach. The SSPM transforms a random domain into a random force-term in the original deterministic/stochastic governing PDEs. The (deterministic) smoothed profile method was developed in [21–27]. An error analysis of a semi-implicit extension of this method, which is implemented in the current study, can be found in [28]. The SSPM uses a smoothly spreading interface layer to represent rough boundaries; within this layer a transition from rigid body motion to fluid motion takes place. Then, the velocity inside each random domain is updated by integrating a "penalty" body force to ensure the rigid presence of the geometry.

This paper is organized as follows: the representation of random roughness is given in Section 2 using the stochastic smoothed profile method (SSPM) in conjunction with the Karhunen–Loéve expansions to model the rough wall-boundaries. Then, in Section 3, the SSPM formulation of stochastic Navier–Stokes equations is obtained by introducing an extra random force-term. In Section 4, the stiffly-stable high order splitting scheme is explained step-by-step to perform the time-integration of the stochastic Navier–Stokes equations. We represent the spatial and the stochastic discretization of the governing equations in the physical space using the spectral/*hp* element method, and in the random space by means of multi-element probabilistic collocation method (ME-PCM). In Section 5, the numerical results are discussed. First, an external flow i.e., flow past a cylinder with random wall-roughness is considered, for which a stochastic harmonic model is obtained for the corresponding asymptotic behaviour of the lift coefficient. As an internal flow test case, Stokes flow in a channel with rough walls is then numerically solved. The mean and the standard deviation of the velocity field in the rough channel are compared to those obtained by a different method, called stochastic mapping approach (SMA). We end this paper by summary and conclusions. An appendix is also included for further explanation of SMA.

2. Representation of random domains

Consider a bounded spatial domain $D = \mathcal{D}^f \cup \mathcal{D}^w$, where $\mathcal{D}^f$ denotes the fluid domain and $\mathcal{D}^w$ represents the entire wall domain of the problem. In this context, $\mathcal{D}^f$ and $\mathcal{D}^w$ are disjoint, moreover, $\mathcal{D}^w$ generally consists of N_w non-overlapping wall sub-domains, i.e., $\mathcal{D}^w = \bigcup_{i=1}^{N_w} \mathcal{D}^{w_i}$. The intersection of $\mathcal{D}^f$ and each wall sub-domain $\mathcal{D}^{w_i}$ is referred to as a wall-boundary segment denoted by $\mathcal{D}_{B_i}$ (lines and surfaces in two and three spatial dimensions). Flow problems involving random wall-roughness render $\mathcal{D}^w$ and, therefore, $\mathcal{D}^f$ stochastic through the common random boundary $\mathcal{D}_{B_i}$ between the fluid domain $\mathcal{D}^f$ and each wall sub-domain $\mathcal{D}^{w_i}$. For example, a schematic external flow past two arbitrary objects is shown in Fig. 1, where the total SSPM spatial domain D is decomposed into the fluid domain $\mathcal{D}^f$ and the wall-domain $\mathcal{D}^w$, also $\mathcal{D}^w$ is consisting of two *random* wall sub-domains i.e., $N_w = 2$.

Let $(\Omega, \mathcal{F}, \mathbb{P})$ be a complete probability space, where Ω is the space of events, $\mathcal{F} \subset 2^\Omega$ denotes the σ-algebra of sets in Ω, and $\mathbb{P}$ is the probability measure. The SSPM represents the random geometry of the ith wall sub-domain, $\mathcal{D}_{w_i}$, $\mathbb{P}$-almost surely (a.s.), by a particular smoothed profile called a stochastic indicator/concentration function,

$$\phi_i(\mathbf{x}; \omega) = \frac{1}{2} \tanh \left[-\frac{d_i(\mathbf{x}; \omega)}{\eta_i} \right] + \frac{1}{2}, \quad \omega \in \Omega, \tag{1}$$

where $\mathbf{x} \in D$ represents the spatial coordinate and η_i denotes the interface thickness of the ith wall sub-domain $\mathcal{D}_{w_i}$. Here, $d_i(\mathbf{x}; \omega)$
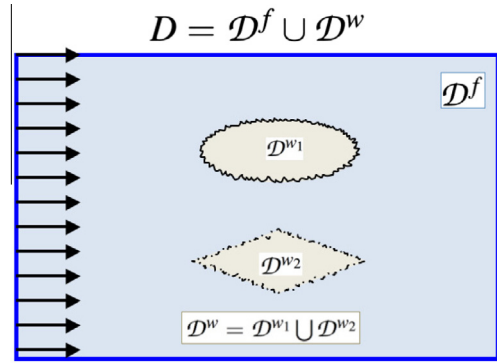

Fig. 1. Schematics of the total SSPM spatial domain D, which is decomposed into the fluid domain $\mathcal{D}^f$ and the wall-domain $\mathcal{D}^w$, where $\mathcal{D}^w$ is consisting of two *random* wall sub-domains $\mathcal{D}^{w_1}$ and $\mathcal{D}^{w_2}$ whose random boundaries are $\mathcal{D}_{B_1}$ (solid line) and $\mathcal{D}_{B_2}$ (dashed line), respectively.

is the *signed* distance to the ith random wall sub-domain $\mathcal{D}_{w_i}$ with positive value outside and negative value inside $\mathcal{D}_{w_i}$. The randomness of $\mathcal{D}_{w_i}$ renders d_i random. In general, a closest-point searching procedure should be used to find $d_i(\mathbf{x}; \omega)$. This technique of representing a random geometry in the context of a fixed canonical topology follows the spirit of Level Set Method (LSM), rendered stochastic (see e.g., [29]). If $\mathcal{D}_{B_i}$ is a boundary of a canonical domain (e.g., a cylinder, sphere, or plane), then one can use the following procedure to calculate $d_i(\mathbf{x}; \omega)$.

Suppose that a random boundary segment $\mathcal{D}_{B_i}$ can be represented by a random field $h(\mathbf{s}; \omega)$ that has the ensemble mean $\mathbb{E}\{h(\mathbf{s})\} = \bar{h}(\mathbf{s})$, finite variance $\mathbb{E}\{[h(\mathbf{s}) - \bar{h}(\mathbf{s})]^2\}$, and covariance $C_h(\mathbf{s}_1, \mathbf{s}_2) = \mathbb{E}\{[h(\mathbf{s}_1) - \bar{h}(\mathbf{s}_1)][h(\mathbf{s}_2) - \bar{h}(\mathbf{s}_2)]\}$. Then a Karhunen–Loève (KL) expansion of $h(\mathbf{s}; \omega)$ takes the form

$$h(\mathbf{s}; \omega) = \bar{h}(\mathbf{s}) + \sum_{k=1}^{\infty} \sqrt{\lambda_k} \Psi_k(\mathbf{s}) \xi_k(\omega), \tag{2}$$

where $\xi_k(\omega)$ are mutually uncorrelated random variables with zero mean and unit variance, while $\psi_k(\mathbf{s})$ and λ_k are the eigenfunction and eigenvalues of the covariance kernel $C_h(\mathbf{s}_1, \mathbf{s}_2)$. Following [30], we obtain the covariance kernel C_h and its eigenvalues and eigenfunctions, by solving a stochastic Helmholtz equation

$$\triangle h - m^2 h = f(\mathbf{s}; \omega), \tag{3}$$

where the random forcing $f(\mathbf{s}; \omega)$ is a white-noise process with zero mean and unit variance. For periodic boundary conditions, the eigenvalues and eigenvectors of (3) form a Fourier series, so that the KL expansion (2) is replaced with its sine Fourier series version

$$h(\mathbf{s}; \omega) = \bar{h}(\mathbf{s}) + \sum_{k=1}^{\infty} b_k \sin \left(\frac{2k\pi \mathbf{s}}{T} \right) \xi_k(\omega), \tag{4}$$

in which the random variables $\xi_k(\omega)$ are chosen to be uniformly distributed, T is the length of the process along the $\mathbf{x}$-axis, and

$$b_n = \frac{2}{\sqrt{T}\ell^2} \left[1 + \left(\frac{2\pi n}{T\ell} \right)^2 \right]^{-1}, \tag{5}$$

where $\ell = T/A$ and A is the correlation length of $h(\mathbf{x}; \omega)$. To ensure that the random variables $\xi_k(\omega)$ have zero mean and unit variance, we define them on $\xi_k(\omega) \in \left[-\sqrt{3}, \sqrt{3} \right]$.

To render (4) computable, we truncate the infinite series with a prescribed fraction of the energy of the process. Let h_m denote the truncated expansion, and assume that $\bar{h}_m(\mathbf{x}) = 0$. Furthermore, we introduce a non-dimensional roughness height

$$y(\mathbf{s}, \omega) = \epsilon \frac{h_m}{\mu}, \quad \mu = \max_{\mathbf{s}} [\sigma_{h_m}], \tag{6}$$

where ϵ is the amplitude of the roughness height, and σ_{h_m} is the standard deviation of h_m.

In lieu of example, we demonstrate how the random signed distance $d_i(x; \omega)$ can be constructed for a stationary rough cylinder. In this case, the deterministic signed distance is $d_i(x) = | \mathbf{x} - \mathbf{R}_i | - a_i$, where a_i is the cylinder's radius, and $\mathbf{R}_i$ is the position vector of the cylinder's center. Let us assume that the roughness exhibits no variation along the length of the cylinder. Then, using the KL expansion (4) to represent the random roughness of the cylinder's surface in the radial direction (i.e., $\mathbf{s}$ in (2)), we express the stochastic indicator function (1) as

$$\phi_i(\mathbf{x}; \omega) = \frac{1}{2} \tanh \left[\frac{a_i + y(\mathbf{s}; \omega) - | \mathbf{x} - \mathbf{R}_i |}{\eta_i} \right] + \frac{1}{2}. \tag{7}$$

By construction, $\phi_i(\mathbf{x}; \omega) = 1$ inside the wall-geometry ($\mathbf{x} \in \mathcal{D}_{w_i}$) and $= 0$ inside the fluid field ($\mathbf{x} \in \mathcal{D}_f$). The transitional zone, wherein $\phi_i(\mathbf{x}; \omega)$ varies smoothly between 1 and 0, defines the rough segments $\mathcal{D}_{B_i}$. For each of N_w rough domains $\mathcal{D}_{w_i}$ ($i = 1, \ldots, N_w$), we compute an indicator function ϕ_i and obtain the total concentration field as

$$\phi(\mathbf{x}; \omega) = \sum_{i=1}^{N_w} \phi_i(\mathbf{x}; \omega). \tag{8}$$

3. SSPM formulation of stochastic Navier–Stokes equations

Inside the random domain $\mathcal{D}^f$, we consider flow of an incompressible Newtonian fluid with density ρ and kinematic viscosity ν. The flow is described by a combination of the continuity and Navier–Stokes (NS) equations,

$$\nabla \cdot \mathbf{u}_f = 0 \quad (\mathbf{x}, t; \omega) \in \mathcal{D}^f \times \mathbb{R}^+ \times \Omega, \tag{9a}$$

$$\frac{\partial \mathbf{u}_f}{\partial t} + (\mathbf{u}_f \cdot \nabla)\mathbf{u}_f = -\frac{1}{\rho}\nabla p + \mathbf{g} + \nu\nabla^2 \mathbf{u}_f \quad (\mathbf{x}, t; \omega) \in \mathcal{D}^f \times \mathbb{R}^+ \times \Omega, \tag{9b}$$

where $\mathbf{g}$ is an external force (e.g., gravity), $p(\mathbf{x}, t; \omega)$ is the fluid pressure, and $\mathbf{u}_f(\mathbf{x}, t; \omega)$ is the fluid velocity. Randomness of the state variables p and $\mathbf{u}_f$ stems from uncertainty in the flow domain $\mathcal{D}(\omega)$. For the sake of generality, we allow the random domain $\mathcal{D}_w(t; \omega) = \bigcup_{k=1}^{N_w} \mathcal{D}_{B_k}(t; \omega)$ of the flow domain $\mathcal{D}^f(t; \omega)$ to vary with time t.

Let $\mathbf{V}_i$ and $\mathbf{W}_i$ denote the translational and angular velocities of $\mathcal{D}_{w_i}(t; \omega)$, respectively. Then $\mathbf{u}_w(\mathbf{x}, t; \omega)$, the velocity of the entire wall-domain with random boundaries $\mathcal{D}_B(t; \omega)$, is constructed from rigid motion of the N_w bodies as

$$\phi(\mathbf{x}, t; \omega)\mathbf{u}_w(\mathbf{x}, t; \omega) = \sum_{i=1}^{N_w} \{\mathbf{V}_i(t) + \mathbf{W}_i(t) \times [\mathbf{x} - \mathbf{R}_i(t)]\}\phi_i(\mathbf{x}, t; \omega), \tag{10}$$

where $\mathbf{R}_i$ ($i = 1, \ldots, N_w$) is the position vector of the centroid of the ith sub-domain with random boundaries. Assuming that envelopes of the boundary segments $\mathcal{D}_{w_i}(t; \omega)$ ($i = 1, \ldots, N_w$) do not overlap, one can show that $\phi_i \nabla \phi_j = 0$ for $\forall i \neq j$. This condition is translated into the impermeability of wall-boundaries. Consequently, $\nabla \cdot (\phi \mathbf{u}_w) \equiv 0$, which ensures the incompressibility of the velocity field inside the wall-domain.

Finally, the *total velocity* $\mathbf{u}(\mathbf{x}, t; \omega)$ is defined as a superposition of the wall-domain velocity $\mathbf{u}_w$ and the fluid velocity $\mathbf{u}_f$,

$$\mathbf{u}(\mathbf{x}, t; \omega) = \phi(\mathbf{x}, t; \omega)\mathbf{u}_w(\mathbf{x}, t; \omega) + [1 - \phi(\mathbf{x}, t; \omega)]\mathbf{u}_f(\mathbf{x}, t; \omega). \tag{11}$$

Inside the random wall domain ($\phi = 1$), $\mathbf{u} = \mathbf{u}_w$, i.e., the total velocity equals the wall velocity. In the interfacial domain ($0 < \phi < 1$), the total velocity changes smoothly from $\mathbf{u}_w$ to $\mathbf{u}_f$. This approach implicitly imposes the no-slip and no-penetration boundary

conditions along the random wall domains presented by the indicator function (1), see also [28].

SSPM solves the NS equations for the total velocity $\mathbf{u}(\mathbf{x}, t; \omega)$ in a deterministic domain $D \subset \mathbb{R}^d$ ($d = 2$ or 3, and $\mathcal{D}^f \subset D$),

$$\nabla \cdot \mathbf{u} = 0 \quad (\mathbf{x}, t; \omega) \in D \times \mathbb{R}^+ \times \Omega, \tag{12a}$$

$$\frac{\partial \mathbf{u}}{\partial t} + (\mathbf{u} \cdot \nabla)\mathbf{u} = -\frac{1}{\rho}\nabla p + \mathbf{g} + \nu\nabla^2 \mathbf{u} + \mathbf{f} \quad (\mathbf{x}, t; \omega) \in D \times \mathbb{R}^+ \times \Omega, \tag{12b}$$

where $\mathbf{f}(\mathbf{x}, t; \omega)$ is a random force density term that represents interactions between the random boundaries and the fluid. We postpone the precise definition of $\mathbf{f}(\mathbf{x}, t; \omega)$ till the following section. Here it suffices to say that $\mathbf{f}(\mathbf{x}, t; \omega)$ is required to satisfy the *finite-dimensional noise* assumption [31]. In other words, the random force term $\mathbf{f}$ must be represented in a finite-dimensional probability space by truncation of the KL expansion as discussed in Section 2.

Key advantages of SSPM now become apparent. First, it replaces the task of solving PDEs on complex (possibly evolving in time) random domains $\mathcal{D}(\omega, t)$ with a more tractable problem of solving stochastic PDEs on canonical deterministic domains D. In the case of flow past an obstacle (e.g., cylinder) with random roughness, the free space $\mathbb{R}^d$ might play the role of D. Second, unlike mapping-based approaches [12,13,20,6], SSPM does not involve a domain transformation that can be computationally demanding. A comparison of SSPM and the mapping-based approach [6] is provided in Section 5.3.

4. Discretization of stochastic Navier–Stokes equations

4.1. Time integration

Let τ denote the length of the simulation time. In order to enhance the stability and temporal accuracy, we use a semi-implicit method with a stiffly-stable high-order *splitting* scheme [32] that was implemented in the context of the smoothed profile method in [28]. In this velocity-correction splitting scheme, the fields at time level n are advanced over a time step Δt through the four sequential sub-steps outlined below.

4.1.1. Advection step
An intermediate velocity field $\mathbf{u}^s$ is computed by using a standard stiffly-stable scheme to integrate the non-linear term and the body force,

$$\mathbf{u}^s = \sum_{m=0}^{J_e-1} \alpha_m \mathbf{u}^{n-m} + \Delta t \sum_{m=0}^{J_e-1} \beta_m [-(\mathbf{u} \cdot \nabla)\mathbf{u} + \mathbf{g}]^{n-m} \quad \text{in} \quad D \times \Omega. \tag{13}$$

Here α_m and β_m are the coefficients of the integration method [33, p. 264], $\mathbf{u}^{n-m}$ and $\mathbf{g}^{n-m}$ denote the values of $\mathbf{u}$ and $\mathbf{g}$ at the previous time steps, and J_e is the order of integration.

4.1.2. Pressure step
An intermediate pressure $\tilde{p}(\mathbf{x}, t; \omega)$ is computed by solving

$$\nabla^2 \tilde{p} = \frac{\rho}{\Delta t}\nabla \cdot (\mathbf{u}^s) \quad D \times \Omega, \tag{14}$$

subject to the Neumann boundary condition

$$\mathbf{n} \cdot \nabla \tilde{p} = \sum_{m=0}^{J_e-1} \beta_m \mathbf{n} \cdot [-(\mathbf{u} \cdot \nabla)\mathbf{u} + \mathbf{g} - \nu\nabla \times (\nabla \times \mathbf{u})]^{n-m}, \tag{15}$$

on all velocity Dirichlet boundaries defined on D. Then the velocity is updated from $\mathbf{u}^s$ to $\mathbf{u}^{ss}$ by accounting for the contribution of the pressure term,

$$\mathbf{u}^{ss} = \mathbf{u}^s - \frac{\Delta t}{\rho}\nabla\tilde{p} \quad \text{in} \quad D \times \Omega. \tag{16}$$

Eqs. (14)–(16) are derived as follows. Following the velocity-correction splitting scheme [33], (14) is derived from (16) by accounting for the continuity equation $\nabla \cdot \mathbf{u}^{ss} = 0$. The boundary condition (15) is not defined on the random boundary segments because in the view of the SSPM they are treated indirectly by means of the random force $\mathbf{f}$.

4.1.3. Viscous step

Treating the viscous term implicitly, we obtain the intermediate velocity $\mathbf{u}^*$ from $\mathbf{u}^{ss}$ by solving

$$\left(\nabla^2 - \frac{\gamma_0}{\nu\Delta t}\right)\mathbf{u}^* = -\frac{\mathbf{u}^{ss}}{\nu\Delta t} \quad \text{in} \quad D \times \Omega, \tag{17}$$

where $\gamma_0 = \sum_{m=0}^{J_e - 1}\alpha_m$ is the scaled coefficient of the stiffly-stable scheme.

4.1.4. Velocity update due to rigid-body motion constraint

The momentum change of a rigid body (and its interfacial domain) equals the time integral of both the hydrodynamic force and the external force, i.e.,

$$\int_{t^n}^{t^{n+1}} \mathbf{f}\,\mathrm{d}t = \phi(\mathbf{u}_w - u^*), \tag{18}$$

where u^* denotes the velocity field obtained in the previous step without considering the presence of the wall-domain forcing term. This is the key to our stochastic transformation of a random boundary (rigid-body wall) into an additional random force density term in the NS Eqs. (12b). The hydrodynamic force ($\mathbf{F}$) and torque ($\mathbf{N}$) on the random domain exerted by the ambient fluid are derived from the momentum conservation between the wall $\mathcal{D}^{w_i}$ and the fluid $\mathcal{D}^f$ as

$$\mathbf{F}_i^{n+1} = \frac{1}{\Delta t}\int_D \rho\phi_i^{n+1}(\mathbf{u}^* - \mathbf{u}_w^n)\mathrm{d}\mathbf{x} - \int_D \phi_i^{n+1}\rho\mathbf{g}^{n+1}\mathrm{d}\mathbf{x} \tag{19a}$$

$$\mathbf{N}_i^{n+1} = \frac{1}{\Delta t}\int_D \mathbf{r}_i^{n+1} \times [\rho\phi_i^{n+1}(\mathbf{u}^* - \mathbf{u}_w^n)]\mathrm{d}\mathbf{x} - \int_D \phi_i^{n+1}\mathbf{r}_i^{n+1} \times (\rho\mathbf{g}^{n+1})\mathrm{d}\mathbf{x}, \tag{19b}$$

where $\mathbf{r}_i^{n+1}$ is the distance vector from the instantaneous rotational reference point on the ith wall-body $\mathcal{D}^{w_i}$ to any point $\mathbf{x} \in D$.

Next, the translational ($\mathbf{V}_i$) and angular ($\mathbf{W}_i$) velocities of $\mathcal{D}^{w_i}$ are updated using Newton's equations as

$$\mathbf{V}_i^{n+1} = \mathbf{V}_i^n + M_i^{-1} \cdot \Delta t \cdot \sum_{q=0}^{Je} a_q \cdot (\mathbf{F}_{h_i}^{n-q} + \mathbf{F}_{ext_i}^{n-q}) \tag{20a}$$

$$\mathbf{W}_i^{n+1} = \mathbf{W}_i^n + I_i^{-1} \cdot \Delta t \cdot \sum_{q=0}^{Je} a_q \cdot (\mathbf{N}_{h_i}^{n-q} + \mathbf{N}_{ext_i}^{n-q}), \tag{20b}$$

where M_i and I_i are the mass and the moment of inertia of the ith wall sub-domain, a_q are the coefficients from a Adam–Bashforth scheme. Here $\mathbf{F}_{ext_i}^{n-q}$ and $\mathbf{N}_{ext_i}^{n-q}$ are, respectively, the external force and torque, also $\mathbf{F}_{h_i}^{n-q}$ and $\mathbf{N}_{h_i}^{n-q}$ denote the hydrodynamic force and torque defined in (19), exerting on the ith sub-wall domain at previous time steps. Then, the corresponding updated velocity field $\mathbf{u}_w^{n+1}$ is calculated from (10). The random forcing in (12b) at time level $n + 1$ is obtained from (18) as

$$\mathbf{f}^{n+1} \approx \frac{\mathbf{u}_w^{n+1} - \mathbf{u}^*}{\Delta t}\phi^{n+1}. \tag{21}$$

This relation demonstrates that the random forcing $\mathbf{f}(\mathbf{x}, t; \omega)$ represents a multiplicative noise that SSPM is conceptually similar to penalty methods [34,35].

Finally, the total velocity field $\mathbf{u}^{n+1}$ is obtained by enforcing the rigid-body motion constraint using the random forcing in (21),

$$\frac{\mathbf{u}^{n+1} - \mathbf{u}^*}{\Delta t} = \mathbf{f}^{n+1} - \nabla p_w, \quad \text{in} \quad D \times \Omega, \tag{22}$$

Here $p_w(\mathbf{x}, t; \omega)$ is the extra pressure due to rigidity of the wall-body geometry. It satisfies a Poisson equation

$$\nabla^2 p_w = \nabla \cdot \mathbf{f}^{n+1} \quad \text{in} \quad D \times \Omega, \tag{23a}$$

which is obtained by taking the divergence of (22). Corresponding boundary conditions for p_w along the velocity Dirichlet boundary are

$$\mathbf{n} \cdot \nabla p_w = \mathbf{n} \cdot \mathbf{f}^{n+1}. \tag{23b}$$

The total pressure $p(\mathbf{x}, t; \omega)$ is calculated as $p = p_w + p^*$.

4.2. Spatial discretization

We use the spectral/hp element method [33] to discretize the SSPM equations in the deterministic domain D. This method enables us to accurately represent deterministic fixed rigid boundaries of the flow domain, while using SSPM to represent the roughness. (However, any discretization method with adaptive refinement near the wall is appropriate.) We accomplish this by partitioning $\mathcal{D}$ into non-overlapping elements $\mathcal{D} = \bigcup_{e=1}^{N_{el}}\mathcal{D}^e$. By constructing the standard element $\mathcal{D}^{st}$, the local coordinates in the standard element ($\zeta \in \mathcal{D}^{st}$) can be mapped to the global coordinate in any elemental domain ($\mathbf{x} \in \mathcal{D}^e$) by an iso-parametric transformation $\mathbf{x} = \chi^e(\zeta)$.

In the p-refinement step, a polynomial expansion of order P is employed within the standard element to construct an approximate solution u^δ as

$$u^\delta(\mathbf{x}) = \sum_{e=1}^{N_{el}}\sum_{j=1}^P \hat{u}_j^e\Phi_j^e(\zeta) = \sum_{i=0}^{N_{dof}}\hat{u}_i\Phi_i(\mathbf{x}), \tag{24}$$

where N_{el} represents the total number of elements in D, and N_{dof} denotes the total degrees of freedom i.e., modal coefficients in the solution expansion. Here $\zeta = [\chi^e]^{-1}(\mathbf{x})$ is the local coordinate, $\Phi_i^e(\zeta)$ are the local expansion modes, and $\Phi_i(\mathbf{x})$ are the global modes derived from the global assembly of the local modes [33]. Both *modal* and *nodal* basis can be used for the basis $\Phi_j^e(\zeta)$. In this study, a modal expansion is utilized in conjunction with a Galerkin projection to solve (14), (17) and (23a), while a nodal expansion is used in conjunction with a collocation projection of (13).

The updating step (22) can be done by either collocation or a Galerkin projection. The former is more efficient but might result in a numerical solution that is discontinuous at some element boundaries. The latter guarantees $\mathcal{C}^0$ continuity of a numerical solution across the elements through an appropriate choice of the boundary modes. For the modal expansion, we use a semi-orthogonal basis written in terms of the Jacobi polynomials. Finally, we employ the Lagrange–Jacobi polynomials through the Gauss–Lobatto quadrature points for the nodal basis.

4.3. Stochastic discretization

In order to discretize the stochastic NS Eqs. (12) in the random space Ω, we implement a multi-element probabilistic collocation method (ME-PCM), see [36]. The finite-dimensional noise assumption mentioned in Section 3 suggests that the random force $\mathbf{f}(\mathbf{x}, t; \omega)$ can be represented by a finite set of random variables $\{\Xi_1(\omega), \Xi_2(\omega), \ldots, \Xi_N(\omega)\}$ with a known joint probability density function (PDF)

$$\rho(\boldsymbol{\xi}) = \prod_{j=1}^N \rho_j(\xi_j). \tag{25}$$

Then the SSPM formulation of the flow Eqs. (12) can be posed as follows. Find the total velocity $\mathbf{u}(\mathbf{x}, t; \omega) : D \times [0, \tau] \times \Omega \to \mathbb{R}$, such that within the time interval $[0, \tau]$ and $\forall \mathbf{x} \in D$

$$\frac{\partial \mathbf{u}}{\partial t} + (\mathbf{u} \cdot \nabla)\mathbf{u} = -\frac{1}{\rho} \nabla p + \nu \nabla^2 \mathbf{u} + \mathbf{g}$$
$$+ \mathbf{f}[\mathbf{x}, t; \Xi_1(\omega), \Xi_2(\omega), \ldots, \Xi_N(\omega)] \qquad (26)$$

holds $\mathbb{P}$-a.s. Also, $\omega \in \Omega$ subject to the constraints of incompressibility (12a) and the corresponding boundary conditions for $\mathbf{u}(\mathbf{x}, t; \omega)$. According to the Doob–Dynkin lemma [37], the total velocity $\mathbf{u}(\mathbf{x}, t; \omega)$ can be expressed as $\mathbf{u}[\mathbf{x}, t; \Xi(\omega)]$, where $\Xi = (\Xi_1, \Xi_2, \ldots, \Xi_N)$ is a set of N random variables $\Xi_i(\omega)$ $(i = 1, \ldots, N)$ that constitute a mapping of the sample space Ω onto the target space Λ.

Let a random vector $\xi = (\xi_1, \xi_2, \ldots, \xi_N) \in \Lambda = \prod_{m=1}^{N} \Lambda_m$ denote an arbitrary point in the parametric space, where Λ_m is the image of $\Xi_m(\omega)$. Then, problem (26) can be reformulated as follows. Find $\mathbf{u}(\mathbf{x}, t; \xi) : D \times [0, \tau] \times \Lambda \to \mathbb{R}$ such that

$$\frac{\partial \mathbf{u}}{\partial t} + (\mathbf{u} \cdot \nabla)\mathbf{u} = -\frac{1}{\rho} \nabla p + \nu \nabla^2 \mathbf{u} + \mathbf{g} + \mathbf{f}(\mathbf{x}, t; \xi) \qquad (27)$$

holds ρ-a.s. for $\xi(\omega) \in \Lambda$ and $\forall \mathbf{x} \in D$, subject to the constraints of incompressibility (12a) and the corresponding boundary conditions for $\mathbf{u}$. One can think of the solution $\mathbf{u}(\mathbf{x}, t; \xi)$ as a function on Λ, taking values in a proper Banach space $\mathcal{W}(D)$.

Let $\{\mathcal{B}_i\}_{i=1}^{M_e}$ denote a finite collection of M_e non-overlapping open subsets (or elements) of random space Λ, such that $\cup_{i=1}^{M_e} \mathcal{B}_i = \Lambda$ and $\mathcal{B}_i \cap \mathcal{B}_j = \emptyset$ for $i \neq j$. Once a mesh is selected, a set of collocation points $\{\mathbf{q}_k^i\}_{k=1}^{\mathcal{J}}$ is prescribed in each element $\mathcal{B}_i$, where $\mathcal{J}$ represents the number of quadrature points within each element $\mathcal{B}_i$. For simplicity, we consider rectangular elements $\mathcal{B}_i$. It is common to take $\{\mathbf{q}_k^i\}_{k=1}^{\mathcal{J}}$ to be the points of a cubature rule on $\mathcal{B}_i$ with integration weights $\{\mathbf{w}_k^i\}_{k=1}^{\mathcal{J}}$.

Next, the solution $\mathbf{u}$ is collocated on the set of points $\sum_{i=1}^{M_e} \sum_{k=1}^{\mathcal{J}} \{\mathbf{q}_k^i\}$, where M_e denotes the number of elements in the parametric space. In other words, we use the spectral/hp element method described in Section 4.2 to solve a set of deterministic problems, wherein the random force $\mathbf{f}(\mathbf{x}, t; \xi)$ in (27) is replaced with its deterministic counterpart $\mathbf{f}(\mathbf{x}, t; \mathbf{q}_j^i)$. As a result of this collocation procedure, the approximate solution forms a mapping

$$\mathbf{u}_k(\cdot; \mathbf{q}_j^i) : \Lambda \to \mathcal{W}(D), \qquad (28)$$

which highlights the *non-intrusive* nature of the ME-PCM.

Finally, we use the following procedure to construct a global approximant $\tilde{\mathbf{u}}_k(\mathbf{x}, t; \xi)$ from a set of the deterministic solutions $\{\mathbf{u}_k(\mathbf{x}, t, \mathbf{q}_j^i)\}_j^i$. Let $\mathcal{I}_{\mathcal{B}_i}$ denote an interpolation operator. One choice for $\mathcal{I}_{\mathcal{B}_i}$ is to use the tensor product Lagrangian interpolant

$$\mathcal{I}_{\mathcal{B}_i} \mathbf{u}_k(\mathbf{x}, t; \xi) \equiv \mathcal{L}_{\mathcal{B}_i}^{\mathcal{P}} \mathbf{u}_k(\mathbf{x}, t; \xi) = \sum_{j=1}^{\mathcal{J}} \mathbf{u}_k(\mathbf{x}, t; \mathbf{q}_j^i) L_j^i(\xi), \qquad (29)$$
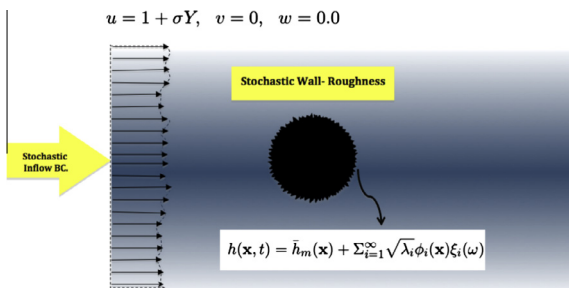
where $\mathcal{P}$ is the polynomial degree in each random space dimension, and $L_j^i(\xi)$ represents the Lagrange polynomial associated with the collocation point $\mathbf{q}_j^i$. In this study, we chose the interpolant $\mathcal{I}_{\mathcal{B}_i}$ to be the isotropic Smolyak sparse grid operator $\mathcal{S}_{\mathcal{B}_i}$ [38]. This choice provides an alternative to the more costly full tensor product rule. The global approximant is computed as

$$\tilde{\mathbf{u}}_k(\mathbf{x}, t; \xi) = \sum_{i=1}^{M_e} \mathcal{I}_{\mathcal{B}_i} \mathbf{u}_k(\mathbf{x}, t; \xi) \mathbb{I}_{\{\omega \in \Omega : \xi(\omega) \in \mathcal{B}_i\}} \quad \forall \mathbf{x} \in D, \quad \forall \xi \in \Lambda, \qquad (30)$$

where $\mathbb{I}_A$ is the characteristic function of a set A.

In order to calculate the statistical moments of $\mathbf{u}$, we define the conditional PDF over ith element in the random space as

$$\rho_{cond}^i(\xi) = \frac{\rho(\xi)}{\int_{\mathcal{B}_i} \rho(\xi) \mathrm{d}\xi}, \quad i = 1, \ldots, M_e. \qquad (31)$$

The *local* mean (expectation) of $\mathbf{u}$ in the ith element is obtained as

$$\mathbb{E}^i[\mathbf{u}] = \mathbb{E}[\mathbf{u} \mid \xi \in \mathcal{B}^i] = \int_{\mathcal{B}^i} \mathbf{u}(\mathbf{x}, t; \xi) \rho_{cond}^i(\xi) \mathrm{d}\xi. \qquad (32)$$

The use of any quadrature method over each element to approximate this integral yields

$$\mathbb{E}_a^i[\tilde{\mathbf{u}}] = \sum_{j=1}^{\mathcal{J}} \mathbf{u}_k(\mathbf{x}, t; \mathbf{q}_j^i) w_j^i \approx \mathbb{E}^i[\tilde{\mathbf{u}}]. \qquad (33)$$

One has to ensure that $\mathbb{E}_a^i$ is defined through the particular choice of collocation grids in ME-PCM. Bayes' theorem allows one to compute an approximate *global* mean by assembling the local mean values on each element in the random space,

$$\mathbb{E}_a[\tilde{\mathbf{u}}](\mathbf{x}, t) = \sum_{i=1}^{M_e} \mathbb{E}_a^i[\tilde{\mathbf{u}}](\mathbf{x}, t) \mathbb{P}[\xi(\omega) \in \mathcal{B}_i] \approx \mathbb{E}[\tilde{\mathbf{u}}](\mathbf{x}, t). \qquad (34)$$

In this study, we use the *uniform* random variables to represent the roughness. This allows us to obtain grids in each element by an affine mapping from a reference element. For general $\rho(\xi)$, grids are element-dependent since $\rho_{cond}^i(\xi)$ are different in each element when the parametric space Λ is decomposed.

5. Numerical results

We apply the SSPM to simulate both *external* and *internal* flows. Section 5.1 presents simulation results for incompressible flow past a circular cylinder with random wall-roughness (external flow). A corresponding stochastic model for the lift coefficient is discussed in Section 5.2 in order to evaluate and verify the asymptotic behavior of statistical moments of the SSPM simulations. Section 5.3 contains simulation results for Stokes flow between two planar plates with rough walls (internal flow).

5.1. Flow past a cylinder with random wall-roughness

Consider incompressible flow past a cylinder with random roughness. For the sake of generality, we allow for uncertain distribution (randomness) of upstream flow velocity (Fig. 2). In the simulation reported below, we set the mean diameter of the cylinder to $\bar{d} = 1.0$ and the corresponding Reynolds number to $Re_{\bar{d}} = 100$. Our focus is on the effects of random roughness on the moments of drag coefficient C_D and lift coefficient C_L.

The radius of the rough cylinder, $h = h(s; \omega)$, where $s = \frac{1}{2} \bar{d} \theta$, varies randomly with the angle $\theta \in [0, 2\pi]$, such that $\mathbb{E}[h] = \frac{1}{2} \bar{d}$. The magnitude of roughness, as quantified by Eq. (6), is set to $\sigma = \epsilon / \mu = 0.1$. We consider the roughness' correlation length ratios $\ell = 0.1, 1.0$ and 2.0. We use the truncated KL expansion (4) with uncorrelated uniformly distributed random variables to approximate the random field in the $h = h(s; \omega)$. Table 1 contains

$$u = 1 + \sigma Y, \quad v = 0, \quad w = 0.0$$

Stochastic Wall-Roughness

Stochastic Inflow BC.

$$h(\mathbf{x}, t) = \bar{h}_m(\mathbf{x}) + \Sigma_{i=1}^{\infty} \sqrt{\lambda_i} \phi_i(\mathbf{x}) \xi_i(\omega)$$

Fig. 2. Flow past a cylinder with random inflow and random roughness.

Table 1
The minimum number of terms in the KL expansion (4), matching $\Sigma_{n=1}^{N}(b_n^2) \geqslant \alpha\Sigma_{n=1}^{\infty}(b_n^2)$ criterion at different $\ell = 0.1, 1.0$ and 2.0.

α (%)	$N(\ell = 0.1)$	$N(\ell = 1.0)$	$N(\ell = 2.0)$
90	1	2	2
95	2	2	3
99	3	4	5

the minimum number of terms that are required to capture 90%, 95%, and 99% of the energy (in the L^2-norm sense), for the correlation length ratios $\ell = 0.1, 1.0$ and 2.0. Fig. 3 shows different realizations of the resulting random surfaces corresponding to the percentage of energy capturing $\alpha = 95\%$.

Obtaining the necessary resolution in both *physical* and *parametric* (random) domains is an important step in capturing the ensemble moments of quantities of interest. In the problem under consideration, the necessary resolution is governed by two parameters: the Reynolds number $Re_{\bar{d}}$, and the correlation ratio ℓ of the random roughness. As $Re_{\bar{d}}$ increases, the inertial term in the NS equations becomes more important, leading to formation of eddies of wider range of length scales [39]. Capturing this phenomenon requires higher mesh resolution in the physical space that can be achieved by *hp*-refinement, as discussed in Section 4.2. Our focus is on the effects of randomness encapsulated in the correlation ratio $\ell = T/A$. For a given length of the roughness process (i.e., $T = 2\pi$), ℓ increases as the correlation length A decreases. It should be noted that at the vicinity of the random surface, higher resolution is needed in order to adequately capture the random roughness.

In general, the impact of $Re_{\bar{d}}$ and ℓ on the parametric space resolution can be clarified through the vortex shedding phenomenon. It is well-understood that (see e.g., [40]) the boundary layer on the cylinder becomes more sensitive to wall-roughness perturbations as $Re_{\bar{d}}$ increases. This would render the separation point of the boundary layer more stochastic, which translates into a more random vortex shedding dynamics behind the cylinder. Therefore, one needs to increase the resolution in the parametric space in order to accurately calculate the moments of the lift coefficient C_{L}. However, in the laminar flow past cylinder the necessary resolution for the parametric space is mostly affected by the correlation length ratio ℓ rather than $Re_{\bar{d}}$.

Consider first the case where the cylinder's surface is the only source of uncertainty, i.e., the upstream velocity $\mathbf{U} = (u, v, w)^{\top}$ is deterministic. We set the corresponding inflow boundary condition to $u = 1, v = 0$, and $w = 0$. Our quantity of interest in the lift coefficient C_{L} defined as

$$C_L = \frac{F_y}{\frac{1}{2}\rho U_{\infty}\bar{d}}, \tag{35}$$

where F_y is the vertical component of the force obtained by (19a), U_{∞} represents the horizontal component of the upstream velocity.

Fig. 4 shows the mean and variance of the lift coefficient C_{L} computed with the SSPM, which employed different numbers of elements and collocation points in its ME-PCM engine. The mean of C_{L} approaches zero as the number of collocation points $\mathcal{J}$ and the number of elements M_e in the parametric space Γ increases. This demonstrates the convergence in the mean of our simulations. Although not shown here, we found similar convergence of the mean of C_{L} to zero for the correlation ratios $\ell = 0.1$ and 2.0 at the same resolution. The effect of random roughness is to reduce the mean of C_{L} to zero, while C_{L} for a smooth cylinder (deterministic case) exhibits temporal oscillations about zero (Fig. 4).

The variance of C_{L} exhibits temporal fluctuations, reaching a constant level in the oscillating sense for large times (Fig. 4). One can see the significant effect of the *h*-refinement (i.e., number of elements M_e in the parametric space) at the beginning and later *p*-refinement in the convergence of the statistics, particularly the mean.

The correlation ratio ℓ has a noticeable effect on the temporal behavior of the variance of C_{L} at early times, i.e., in the pre-asymptotic regime (Fig. 5). As ℓ increases, the variance of C_{L} exhibits stronger temporal fluctuations with higher peak-to-peak values in the transient (pre-asymptotic) regime. However, the variance of C_{L} tends to almost the same asymptotic value (in the oscillating sense).

The variance of the drag coefficient,

$$C_D = \frac{F_x}{\frac{1}{2}\rho U_{\infty}\bar{d}}, \tag{36}$$

where F_x is the horizontal component of the force obtained by (19a), exhibits milder temporal fluctuations, reaching almost the same asymptotic value (in the oscillating sense) at large times (Fig. 6). Although not shown here, we observed that the ensemble mean of C_D has very low sensitivity to the roughness in the asymptotic regime. This is only true for small height of roughness.

5.2. Stochastic model for C_L

In order to verify our results for the ensemble moments of C_L, we develop a stochastic harmonic model of the asymptotic (large time) behavior of the mean and variance of C_L. The model is based on the observation [41] that the lift force F_L on a smooth cylinder in uniform (deterministic) flow is a harmonic function of time,

$$F_L(t) = \frac{1}{2}\rho U_{\infty}^d \bar{d} C_L, \quad C_L(t) \equiv C_L^m \cos(2\pi\zeta^d t), \tag{37}$$

where U_{∞}^d is the deterministic value of the upstream velocity $\mathbf{U} = (U_{\infty}^d, 0, 0)^{\top}, \bar{d}$ is the mean diameter of the cylinder, C_L^m is the
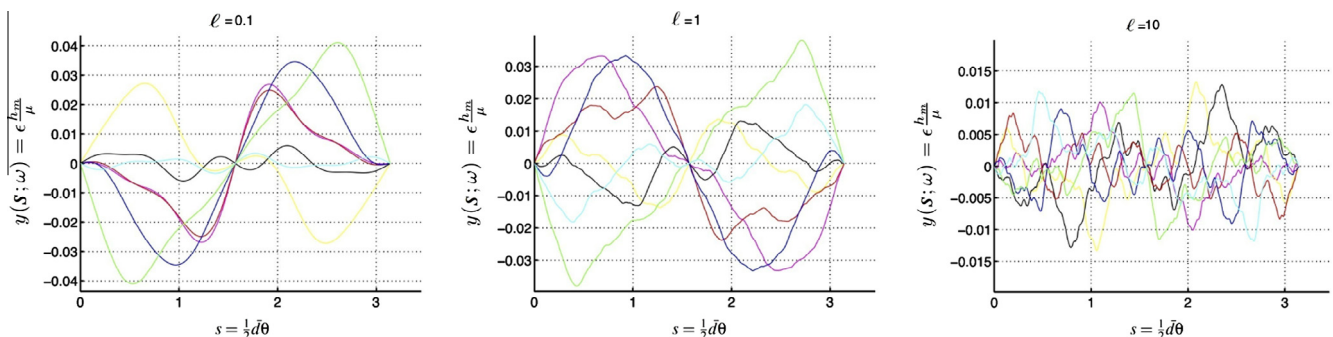
Fig. 3. Realizations of the random wall-roughness along the periphery of the cylinder, corresponding to $\alpha = 95\%$, also $\ell = 0.1$ (left), $\ell = 1.0$ (middle), and $\ell = 10.0$ (right), where $\bar{d} = 1.0$ is the mean diameter of the cylinder and $0 \leqslant \theta \leqslant 2\pi$.
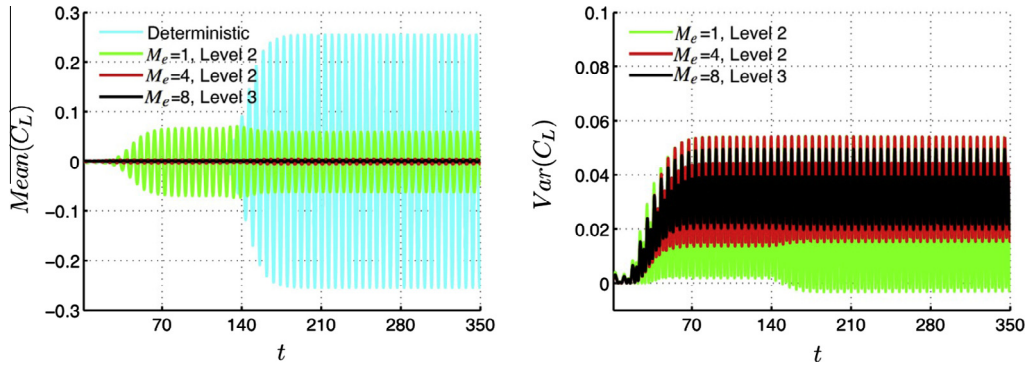
Fig. 4. Temporal behavior of the mean (left) and variance (right) of the lift coefficient C_L computed with several sparse grid levels and different number of elements M_e in the random space. The correlation ratio is set to $\ell = 1$.
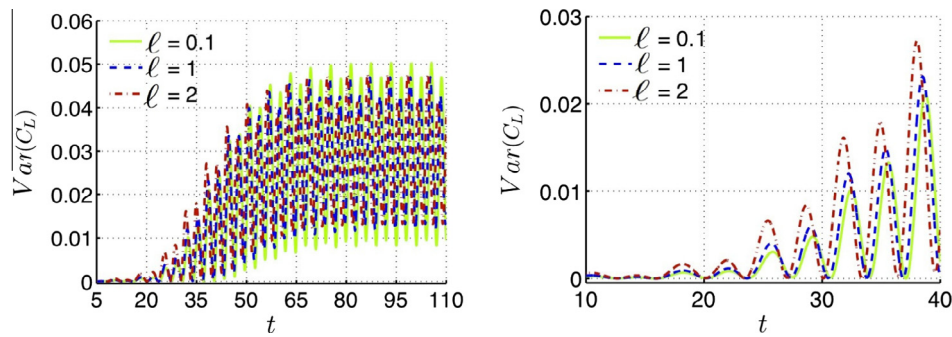

Fig. 5. Temporal behavior of the variance of lift coefficient C_L (left) and its zoomed-in view (right) for $\ell = 0.1, 1.0$ and 2.0 at $Re_d = 100$.
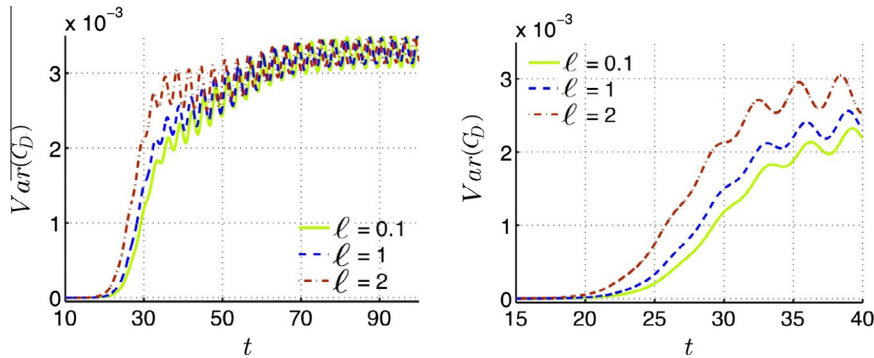

Fig. 6. Temporal behavior of the variance of drag coefficient C_D (left) and its zoomed-in view (right) for $\ell = 0.1, 1.0$ and 2.0 at $Re_d = 100$.

maximum value of the deterministic $C_L(t)$, and ζ^d is the deterministic shedding frequency. Our model accounts for randomness of the cylinder's surface $y(\xi)$ and the upstream velocity $U_\infty(t; Y)$, where $\xi \in \mathbb{R}^N$ and $Y \in \mathbb{R}$ are a set of mutually independent random variables with zero means and unit variances. Replacing the deterministic lift coefficient C_L in (37) with its random counterpart, we obtain

$$C_L(t; Y, \xi) = \mathcal{A} \cos(2\pi \zeta t). \tag{38}$$

Here $\zeta(Y, \xi)$ is the stochastic shedding frequency and

$$\mathcal{A}(Y, \xi) = \mathcal{A}^d \mathbb{I}_{\{\xi = \mathbf{0}\}} + c_1 Y + \mathbf{c}_2 \cdot \xi, \quad \zeta(Y, \xi) = \zeta^d \mathbb{I}_{\{\xi = \mathbf{0}\}} + \alpha Y + \boldsymbol{\beta} \cdot \xi, \tag{39}$$

where $c_1, \mathbf{c}_2, \alpha$ and $\boldsymbol{\beta}$ are non-zero constants. The N-dimensional random vector ξ was introduced in Section 4.3 to represent the random roughness of the cylinder's surface. The one-dimensional random variable Y enters the representation of the separable random upstream velocity U_∞ as

$$U_\infty = (1 + \sigma Y) \mathcal{T}(t), \tag{40}$$

where $\sigma > 0$ is a constant indicating the strength of random fluctuations, and $\mathcal{T}(t)$ denotes an arbitrary (non-zero) function of time.

The ensemble mean of C_L in (38) is given by

$$\mathbb{E}[C_L] = \int_\Gamma C_L(t; y, \mathbf{z}) f_{Y\xi}(y, \mathbf{z}) \mathrm{d}y \mathrm{d}\mathbf{z}, \tag{41}$$

where Γ is the $(N + 1)$-dimensional parameter space, and $f_{Y\xi}(y, \mathbf{z})$ is the joint PDF of Y and ξ that is equivalent to $f_Y(y) f_\xi(\mathbf{z})$ due to the independence of ξ from Y. Combining (38)–(41), decomposing the parametric space into two non-overlapping sets $E_1 = \{0, \mathbf{0}\}$ and $E_2 = \Gamma \setminus E_1$, and representing the integral in (41) as the sum of two corresponding integrals, we obtain

$$\mathbb{E}[C_L] = \int_{E_1} \mathcal{A}^d \cos(2\pi\zeta^d t) f_{Y\xi}(0, \mathbf{0}) \mathrm{d}y \mathrm{d}\mathbf{z}$$
$$+ \int_{E_2} (c_1 y + \mathbf{c}_2 \cdot \mathbf{z}) \cos[2\pi(\alpha y + \boldsymbol{\beta} \cdot \mathbf{z}) t] f_{Y\xi}(y, \mathbf{z}) \mathrm{d}y \mathrm{d}\mathbf{z}. \quad (42)$$

The first integrand in (42) is the deterministic lift coefficient C_L^d, when $Y = 0$ and $\xi = 0$. The corresponding integral is over a set of the Lebesque measure zero, $\lambda(E_1) = 0$. Therefore, the first integral is identically zero. To evaluate the second integral in (42), we expand the cosine term in its integrand, and carrying out the integration over y and $\mathbf{z}$. This yields a time-dependent expression for the ensemble mean of C_L,

$$\mathbb{E}[C_L] = \frac{\sin(2\pi\alpha t)}{\alpha(2\pi t)^2} \sum_i \frac{\sin(2\pi\beta_i t)}{\beta_i}, \quad (43)$$

where β_i's are the components of vector $\boldsymbol{\beta}$ in (39). Since α and β_i are non-zero constants, $\mathbb{E}[C_L] \to 0$ as $t \to \infty$, which is the asymptotic solution obtained with the numerical simulations in the previous section.

The variance of C_L is defined by

$$Var[C_L] = \mathbb{E}[C_L^2] - \mathbb{E}[C_L]^2 = \int_\Gamma C_L^2(t; y, \mathbf{z}) f_{Y\xi}(y, \mathbf{z}) \mathrm{d}y \mathrm{d}\mathbf{z}. \quad (44)$$

Decomposing the parametric space into two non-overlapping sets $E_1 = \{\mathbf{0}\}$ and $E_2 = \Gamma \setminus E_1$, we obtain in the limit of large t

$$Var[C_L] = \frac{1}{2} \int_{E_2} \mathcal{A}^2(y, \mathbf{z}) f_{Y\xi}(y, \mathbf{z}) \mathrm{d}y \mathrm{d}\mathbf{z}. \quad (45)$$

Below we examine the relative importance of the two sources of uncertainty (randomness), random roughness of the cylinder's surface and random upstream velocity, on the statistics of C_L.

5.2.1. Random wall-roughness

When the wall roughness is the only source of uncertainty, (38) and (39) reduce to

$$C_L(t; \xi) = \mathcal{A} \cos(2\pi\zeta t), \quad (46a)$$

where

$$\mathcal{A}(\xi) = \mathcal{A}^d \mathbb{I}_{\{\xi=\mathbf{0}\}} + \mathbf{c}_2 \cdot \xi, \quad \zeta(\xi) = \zeta^d \mathbb{I}_{\{\xi=\mathbf{0}\}} + \boldsymbol{\beta} \cdot \xi. \quad (46b)$$

Then (42) takes the form

$$\mathbb{E}[C_L] = \int_{E_2} (\mathbf{c}_2 \cdot \mathbf{z}) \cos[2\pi(\alpha y + \boldsymbol{\beta} \cdot \mathbf{z}) t] f_\xi(\mathbf{z}) \mathrm{d}\mathbf{z}. \quad (47)$$

If the PDF of the ξ is symmetric with respect to the origin of the random space, then $E_2 = \Gamma \setminus \{\mathbf{0}\}$ is a symmetric hypercube in $\mathbb{R}^N$ and the integrand in (47) is an odd function. Therefore,

$$\mathbb{E}[C_L] = 0, \quad (48)$$

i.e., the stochastic linear model predicts a zero-mean lift coefficient at all times. This result is to be expected since, for flows with $Re_d = 100$, the frequency of shedding is very robust and the stochastic roughness perturbs it only slightly in each realization. This suggests that the linear model (46) is sufficient to verify our numerical simulations.

The roughness amplitude σ affects the laminar boundary layer adjacent to the random surface of the cylinder, where the separation point would be perturbed slightly at low-to-moderate Re_d. At higher Re_d, the separation point changes more chaotically, resulting in a larger stochastic lift force. Thus, the linear model (46) might not be able to correctly predict $\mathbb{E}[C_L]$ at high Re_d. Instead, a quadratic model for the amplitude $\mathcal{A}(t, \xi)$ might be a better choice to predict the asymptotic solution for $\mathbb{E}[C_L]$.
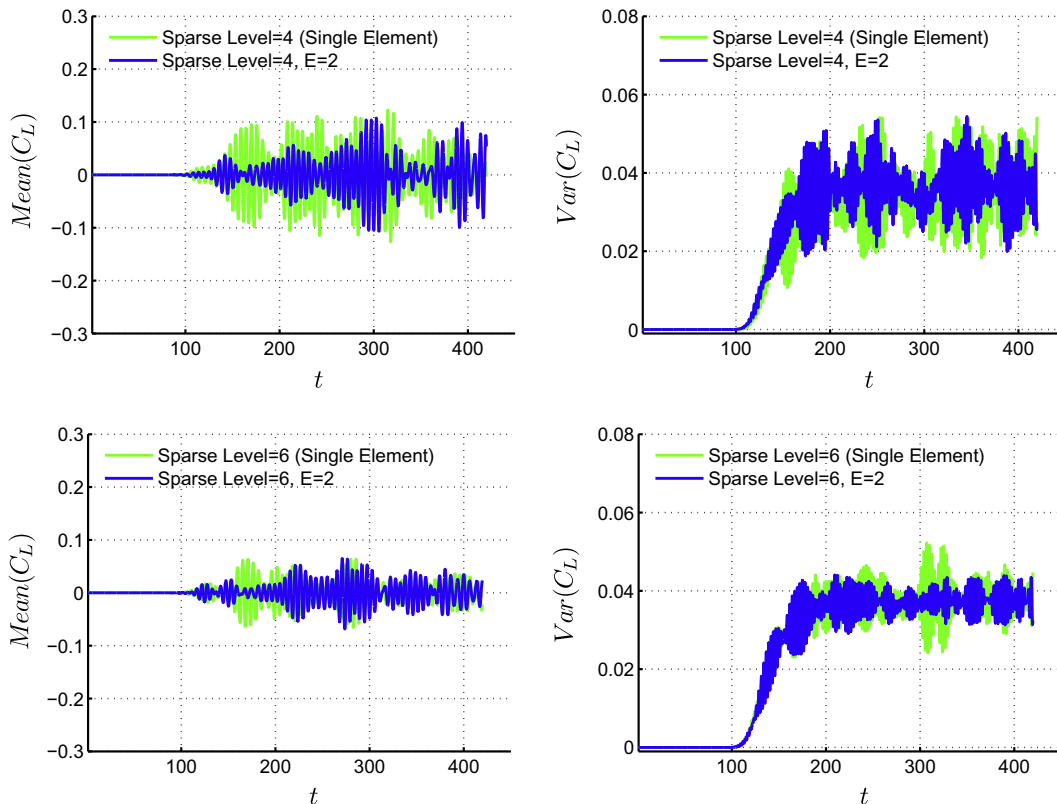

Fig. 7. Temporal behavior of the mean (left column) and variance (right column) of C_L for several sparse grid levels and different number of elements in the random space. Here E denotes the number of elements in the parametric space.

Table 2

The minimum number of terms in the KL expansion (4), matching $\Sigma_{n=1}^{N}(b_n^2) \geqslant \alpha\Sigma_{n=1}^{\infty}(b_n^2)$ criterion at $\ell = 2.0$.

α (%)	$N(l_s = 1, T = 2)$	$N(l_s = 5, T = 10)$
90	2	5
95	2	6
99	4	12

Long-time behavior of the variance of C_L is obtained from (45) as

$$Var[C_L] = \frac{1}{2}\int_{E_2}\mathcal{A}^2(\mathbf{z})f_{\xi}(\mathbf{z})\mathrm{d}\mathbf{z}. \tag{49}$$

This result is consistent with the variance of C_L shown in Fig. 4 (right), where $Var[C_L]$ oscillates about the asymptotic solution. It has been shown in ([42]) that the amplitude of the aforementioned oscillation can be reduced to any arbitrary small range by increasing the resolution in the parametric space.

5.2.2. Random upstream velocity

When the upstream velocity is the only source of uncertainty, (38) and (39) reduce to

$$C_L(t; Y) = \mathcal{A}\cos(2\pi\zeta t), \tag{50a}$$

where

$$\mathcal{A}(y) = \mathcal{A}^d + c_1 Y, \quad \zeta(y) = \zeta^d + \alpha Y. \tag{50b}$$

At late times ($t \to \infty$), (42) and (45) reduce to

$$\mathbb{E}[C_L] = 0, \quad Var[C_L] \to \frac{1}{2}\int_{E_2}\mathcal{A}^2(y)f_Y(y)\mathrm{d}y. \tag{51}$$

These results were compared to those obtained with the numerical simulations of the stochastic NS equations (Section 4). In these simulations, we took the cylinder to be smooth while allowing the upstream velocity to vary in accordance with (40). We also employed the Smolyak formula as a cubature rule, where the collocation points are nested i.e., the collocation points in previous Smolyak sparse levels are fully used in next sparse levels [43–45]. The mean and variance of C_L resulting from these simulations are shown in Fig. 7. Both quantities reach (in the oscillating sense) their respective asymptotic values at later times. The oscillations decrease as the number of collocation points increases.

5.3. Stokes flow in a channel with rough walls

Consider Stokes flow between two parallel plates, one of which is randomly rough. The random flow domain is $\mathcal{D}^f : \{(x, y, z) \in [-T/2, T/2] \times [y_0, \delta] \times [0, \pi]\}$. The upper plate, $y = \delta$, is smooth, while the lower plate is a random surface represented by the truncated expansion (6),

$$y_0(s; \omega) = \epsilon\frac{h_m}{\mu}, \quad \mathbb{E}[h_m] = 0, \tag{52}$$

in which the coordinate s coincides with the x-axis. Let $h_m(x; \omega)$ be periodic in x (i.e., along the flow direction) with period T. This allows us to use the covariance kernel introduced in Section 2 for periodic random processes. In the simulations reported below, we set $\delta = 1, \sigma = 0.2$ or 0.4, and $\ell = T/l_s = 2$ where l_s is the correlation length of $y_0(x; \omega)$. This choice of the correlation length ratio ℓ facilitates representation of the roughness in a higher-dimensional random space at a manageable cost. The number of terms in the KL expansion that are necessary to represent $y_0(x; \omega)$ with a given degree of accuracy (α) are presented in Table 2. Typical realizations of the random plate $y_0(x; \omega)$, for the above-mentioned statistical parameters and the KL expansion that captures $\alpha = 95\%$ of the energy in the L^2-norm sense, are shown in Fig. 8.

A deterministic domain for the SSPM is $D : \{(x, y, z) \in [-T/2, T/2] \times [-\delta, \delta] \times [0, \pi]$. It includes a random wall domain $\mathcal{D}^w : \{(x, y, z) \in [-T/2, T/2] \times [-\delta, y_0] \times [0, \pi]\}$. The flow is driven by the externally applied pressure gradient $-\partial P/\partial x = 2$. Since the stochastic Stokes equations neglect the advection term in the NS equations, the SSPM skips the corresponding step in the time integration (Section 4.1).

In order to verify our SSPM results, we compare them with their counterparts obtained with the mapping approach [6]. The latter is a two-step computational method: first, a random flow domain is mapped onto a deterministic domain; second the transformed stochastic Stokes equations in a deterministic domain are solved using a stochastic Galerkin method (generalized polynomial chaos or gPC) in the probability space and a spectral element method in the physical space. This approach is briefly outlined in A. In both the SSPM and the mapping approach, extensive effort has been made to obtain grid-independent (converged) first and second moments of the horizontal (u) and vertical (v) components of the random velocity vector. The difference between the two solutions is reported in terms of a relative L^2 norm error, for example for horizontal component u,

$$\mathcal{E}(\tilde{u}) = \frac{\|\tilde{u}^{\mathrm{SSPM}} - \tilde{u}^{\mathrm{gPC}}\|_2}{\|\tilde{u}^{\mathrm{SSPM}}\|_2} \times 100\%, \tag{53}$$

where $\tilde{u}^{\mathrm{SSPM}}$ and $\tilde{u}^{\mathrm{gPC}}$ denote the moments of u obtained by the SSPM and the mapping approach (gPC), respectively.

To facilitate the comparison between the two solutions, the SSPM results are presented in the transformed coordinate system (η_1, η_2, η_3), such that $\eta_1 = x, \eta_3 = z$, and $\eta_2 = (y - y_0)/(\delta - y_0)$. This affine mapping transforms the random flow domain $\mathcal{D}^f$ into a deterministic domain $D^t : \{(\eta_1, \eta_2, \eta_3) \in [-T/2, T/2] \times [0, 1] \times [0, \pi]$. The ensemble statistics of $u(x, \eta_2; \omega)$ are displayed at a few cross-
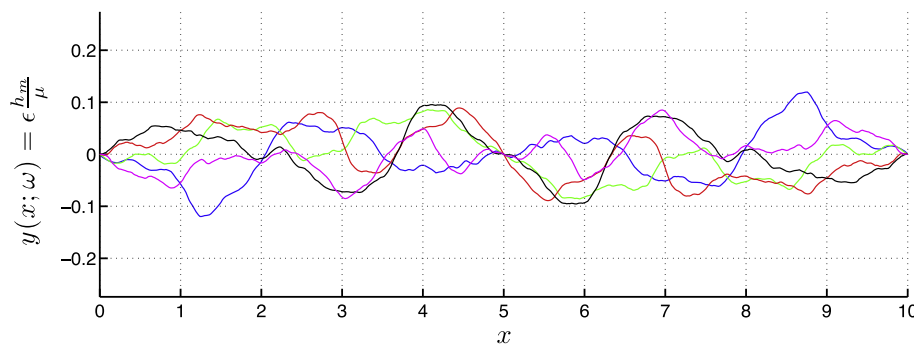

Fig. 8. Realizations of the random bottom plate of the channel for $\ell = 2.0$ and the channel length $T = 10$.
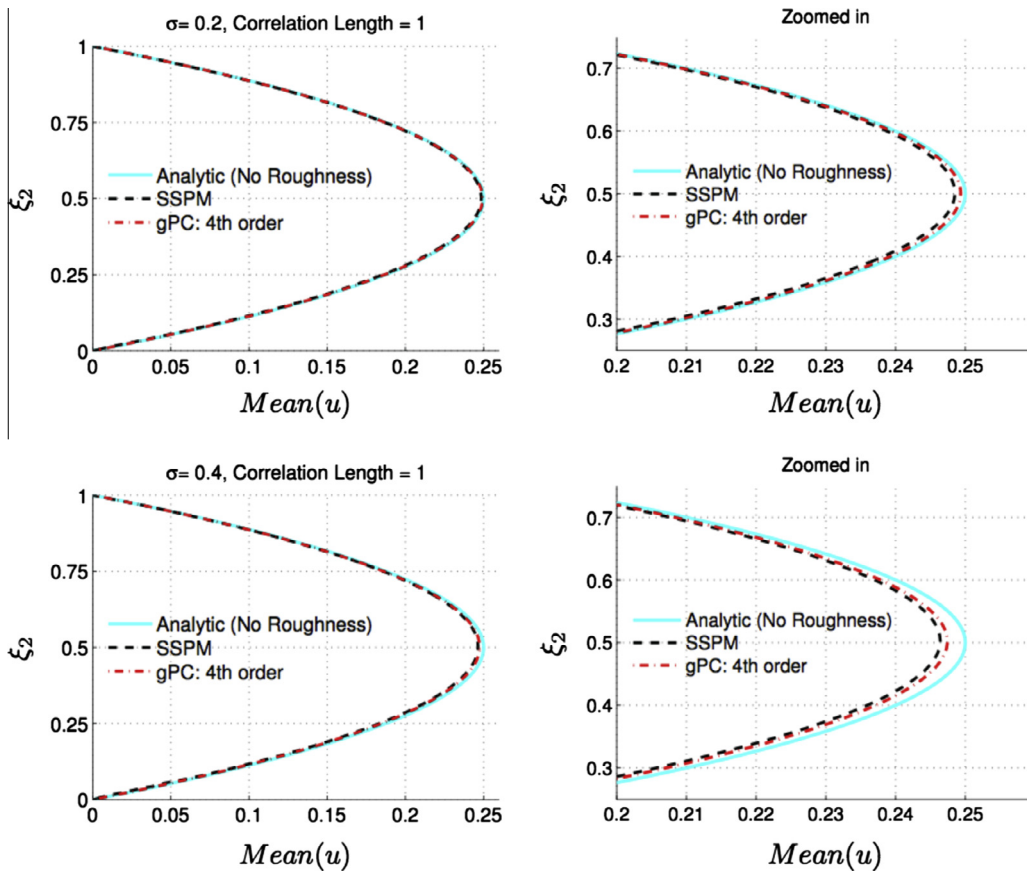
Fig. 9. Mean velocity profiles across the channel width computed at $x = 0.5$ with the SSPM and the mapping approach (gPC) for $l_s = 1$ and either $\sigma = 0.2$ (top) or $\sigma = 0.4$ (bottom). Also shown are the Poiseuille velocity profiles (Analytic) for smooth walls.
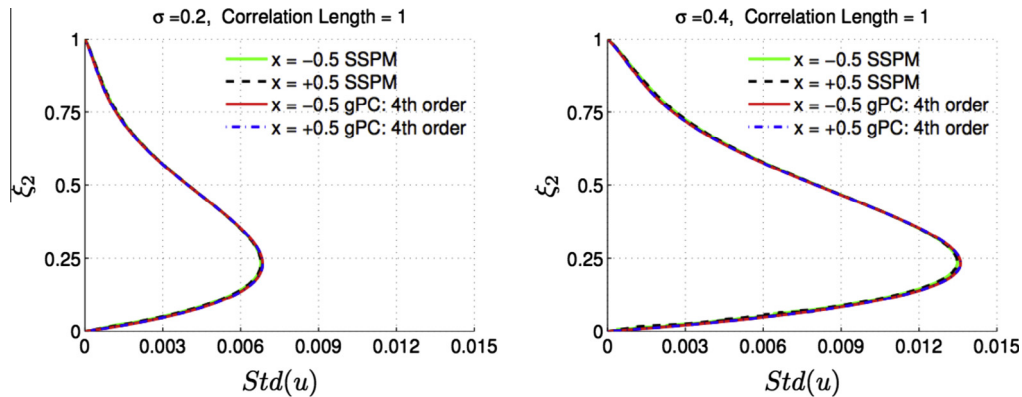

Fig. 10. Standard deviation of u at $x = \pm 0.5$ computed with the SSPM and the mapping approach (gPC) for $l_s = 1$ and $\sigma = 0.4$ (left) or $\sigma = 0.2$ (right).

sections $x = $ const. Since no variation of the roughness along the z-axis is considered, no change in the solution field along the depth of the channel is observed. Based on the covariance kernel and the correlation length utilized, we chose the cross-sections $x = \pm 0.5$ for $T = 2$ and $l_s = 1$, and the cross-sections $x = \pm 2.5$ for $T = 10$ and $l_s = 5$. In both cases, these cross-sections correspond to the locations with the maximum variance of the random roughness $y_0(x, \omega)$.

We present the statistics of the problem across some important cross-sections along the channel. In this study, our choices of correlation length, which are not too small, prohibit any ensemble averaging along the length of the channel. This is so because SSPM

does not involve any transformation of the physical domain, while gPC essentially solves the problem in the transformed domain (see A for more details).

We found the mean of $u(x, \eta_2; \omega)$ to be nearly independent of x. Fig. 9 exhibits the mean velocity profiles across the channel width, $\mathbb{E}[u]$, for $l_s = 1$ and either $\sigma = 0.2$ or 0.4. A visual comparison reveals close agreement between the predictions of $\mathbb{E}[u]$ obtained with the SSPM and the mapping approach (gPC). The two solutions have relative errors $\mathcal{E}\{\mathbb{E}[u]\} = 0.55\%$ for $\sigma = 0.2$ and $\mathcal{E}\{\mathbb{E}[u]\} = 0.72\%$ for $\sigma = 0.4$. As expected, Fig. 9 demonstrates that the mean centerline velocity and, hence, the volumetric flow rate decrease as the wall roughness (σ) increases.
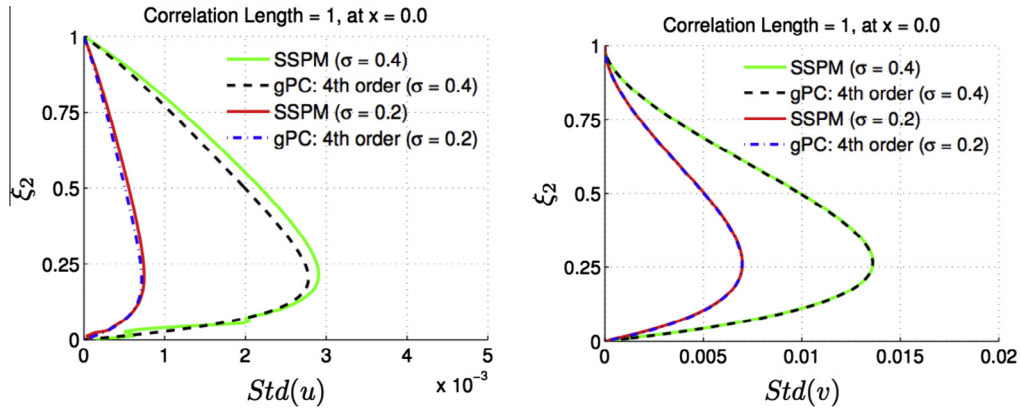
Fig. 11. Standard deviations of u (left) and v (right) at $x = 0.0$ computed with the SSPM and the mapping approach (gPC) for $l_s = 1$ and $\sigma = 0.4$.

Table 3
The relative error $\mathcal{E}$ for the standard deviations of the horizontal (u) and vertical (v) components of flow velocity.

Section	$\sigma = 0.2$		$\sigma = 0.4$	
	$\mathcal{E}\{Std[u]\}, \%$	$\mathcal{E}\{Std[v]\}, \%$	$\mathcal{E}\{Std[u]\}, \%$	$\mathcal{E}\{Std[v]\}, \%$
$x = -0.5$	1.87	7.70	2.02	7.85
$x = 0.0$	7.16	0.53	7.76	0.72
$x = +0.5$	1.72	7.62	2.62	7.66

Fig. 10 shows the standard deviation of $u(x, \eta_2; \omega)$ computed at $x = \pm 0.5$ with the SSPM and the mapping approach (gPC). Since the wall roughness (σ) is highest at $x = \pm 0.5$, one can expect the maximum uncertainty (as quantified by $Std[u]$) to occur at these cross-sections. Fig. 10 reveals that vertical profiles of $Std[u]$ at $x = 0.5$ and $x = -0.5$ coincide, which demonstrates that choosing the simulation domain's length T to satisfy $\ell \equiv T/l_s = 2$ suffices to capture the dynamics of the stochastic Stokes flow. One can also see that the estimates of $Std[u]$ computed with the SSPM and the mapping approach (gPC) are in close agreement. This finding is confirmed quantitatively: the relative errors between the two solutions are $\mathcal{E}\{Std[u]\} = 1.87\%$ for $\sigma = 0.2$ and $\mathcal{E}\{Std[u]\} = 2.62\%$ for $\sigma = 0.4$. The peak of uncertainty, i.e., maximum of $Std[u]$, is shifted from the channel's centerline towards its random wall ($\eta_2 \approx 0.25$). The location of maximum predictive uncertainty is seen to be insensitive to the strength of wall randomness ($\sigma = 0.2$ or 0.4).

As shown in Fig. 8, the random roughness deterministically adopts zero-value in the middle of each process (i.e., at $x = 0.0$). Therefore, one may expect $Std[u]$ to be minimum there. It is shown that $Std[u]$ is non-zero at section $x = 0.0$ due to random fluctuations of the rough wall in its neighborhood. Fig. 11 demonstrates that this is indeed the case. The standard deviation of u at $x = 0.0$ is almost an order of magnitude smaller than its counterpart at $x = 0.5$ (Fig. 10). The relative error between the standard deviations of u computed with the SSPM and the mapping approach is $\mathcal{E}\{Std[u]\} = 7.76\%$.

The presence of random roughness induces vertical fluctuations in flow velocity. While $\mathbb{E}[v] = 0$, the standard deviation of the vertical velocity component $Std[v]$ is appreciable (Fig. 11). In fact, at $x = 0.0$ it is an order of magnitude higher than $Std(u)$. The SSPM and the mapping approach yield the estimates of $Std[u]$ that have a relative error of $\mathcal{E}\{Std[v]\} = 0.72\%$. Table 3 elucidates the latter point further by presenting $\mathcal{E}\{Std[u]\}$ and $\mathcal{E}\{Std[v]\}$ at several cross-section $x = \text{const}$.

To investigate the effects of the correlation length of the surface roughness on the mean flow behavior, we conducted simulations with $l_s = 5$ and $\sigma = 0.4$. The channel's length was changed to
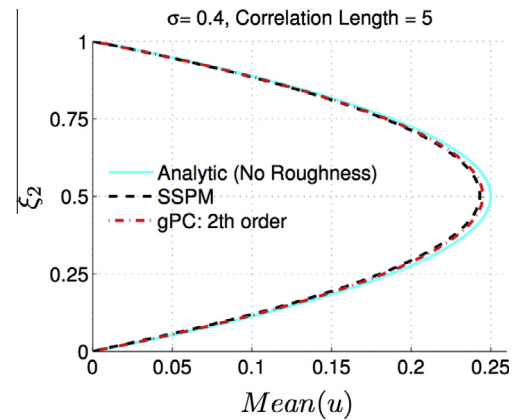

Fig. 12. Mean velocity profiles across the channel width computed at $x = 0.5$ with the SSPM and the mapping approach (gPC) for $l_s = 5.0$ and $\sigma = 0.4$. Also shown is the Poiseuille velocity profile (Analytic) for smooth walls.

$T = 10$ to keep $\ell = T/l_s = 2$. Both approaches underwent a grid-independence study to obtain the resolution in the physical and probability spaces necessary for estimates of the first two ensemble moments to converge. Fig. 12 exhibits the resulting mean flow velocity $\mathbb{E}[u]$ at cross section $x = 0.5$, computed with the SSPM and the mapping approach. The two approaches are in a close agreement, with the relative error of $\mathcal{E}\{\mathbb{E}[u]\} = 0.65\%$. The comparison of Figs. 9 and 12 demonstrates that the flow rate decreases as l_s increases, when the correlation length $\ell = T/l_s = 2$ is kept constant.

Finally, we examine the impact of larger correlation lengths ($l_s = 5$) on the standard deviation of u and v. Fig. 13 presents the estimates of $Std[u]$ and $Std[v]$ computed with the SSPM and the mapping approach. As discussed earlier, the peak positions of $Std(u)$ and $Std(v)$ are insensitive to the strength of the random roughness σ. The comparison of Figs. 11 and 13 demonstrates that the location of maximum uncertainty shifts closer to the random rough wall as l_s decreases, i.e., the wall becomes rougher. The relative error in this simulation is $\mathcal{E}\{Std[u]\} = 2.34\%$ at $x = \pm 2.5$ and $\mathcal{E}\{Std[u]\} = 1.04\%$ at $x = 0.0$.

6. Summary and conclusions

We introduced a stochastic smoothed profile method (SSPM) to solve the Navier–Stokes (NS) equations on random domains. Random boundaries were modeled as a second-order autoregressive process through a Karhunen-Loève (KL) expansion. The SSPM relies
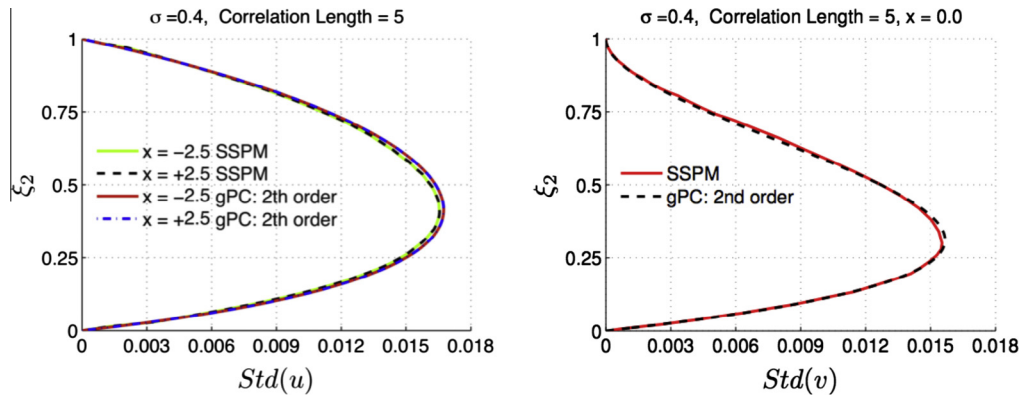
Fig. 13. Standard deviations of u at $x = \pm 2.5$ (left) and v at $x = 0.0$ (right) computed with the SSPM and the mapping approach (gPC) for $l_s = 5.0$ and $\sigma = 0.4$.

on a random indicator function $\phi(\mathbf{x}, t; \omega)$ to transform such boundary-value problems into the stochastic NS equations on deterministic domains. Unlike the stochastic mapping approaches [19,12,13], the SSPM does not require one to construct a numerical map, which can be computationally expensive. Instead, a random force is added to the NS equations. To solve these equations, we used a high-order method that employs a spectral/hp discretization in both physical and random spaces.

We implemented this general approach to model external and internal problems: flow past a rough cylinder and Stokes flow in a channel with rough walls. In the first test-case, we compared the SSPM predictions for the lift coefficient C_L to their counterparts, predicted by a linear stochastic harmonic oscillator model. Next, we used the second problem to verify the SSPM by comparing its predictions with those obtained from Stochastic Mapping Approach (SMA) [6]. The three approaches yielded nearly identical estimates of the statistical moments of quantities of interest, thus demonstrating the accuracy and robustness of the SSPM.

Our analysis leads to the following conclusions regarding the fluid mechanics quantities of interest.

1. Flow past a rough cylinder
   (a) The mean of the lift coefficient C_L for a rough cylinder is zero; the variance of C_L approaches a constant value at large times.
   (b) As the correlation length of roughness decreases, the variance of C_L exhibits stronger temporal fluctuations in the transient (pre-asymptotic) regime. However, the asymptotic value of the variance remains almost the same.
2. Flow in a channel with a rough wall
   (a) Random roughness reduces the volumetric flow rate; this reduction becomes more pronounced as the roughness variance increases and/or its correlation length decreases.
   (b) The peak of uncertainty is shifted from the channel centerline towards its random wall. The location of maximum uncertainty is insensitive to the roughness variance but is affected by its correlation length.

Although the examples considered here deal with PDEs defined on fixed random domains, the SSPM is equally valid for problems in which random domains evolve in time (e.g, free-surface dynamics in random environments [46,19]).

To further discuss the performance of SSPM and SMA which was used for verification, we point out that they both rely on two-step procedures to solve transformed (stochastic or deterministic) PDEs on random domains. In the first step, the governing equations on random domains are transformed into stochastic PDEs on deterministic domains. The SSPM accomplishes this goal by adding a

random force to (stochastic or deterministic) momentum equations, while the SMA maps (analytically or numerically) the random domain onto its canonical deterministic counterpart. In the second step, the resulting stochastic PDEs are solved with standard analytical (e.g., perturbation expansions) or numerical (e.g., polynomial chaos expansions, collocation methods, MCS, etc.) techniques.

Except for problems defined on relatively simple geometries that admit analytical transformations (e.g., flow between two random surfaces or in a tube with randomly varying aperture), numerical procedures involved in the stochastic mapping are computationally demanding. Under these general conditions, the SSPM offers significant computational savings over the SMA. Moreover, the transformed equations in the SMA differ from their original counterparts and therefore might require a modification of numerical codes used to solve the original PDEs. In this sense, the SMA is intrusive regardless of whether its second step (solving stochastic PDEs on deterministic domains) is intrusive or not.

For both methods, without regard to the complexity of the domain, the correlation length of the roughness process can be a bottleneck when it tends to zero. In fact, as the correlation length decreases, the dimension of the parametric space increases. Consequently, the *curse of dimensionality* becomes a barrier for both approaches. For instance, in SMA utilized with the stochastic Galerkin projection, the number of PDEs for the expansion coefficients, $M = \frac{(N+P)!}{N!P!} - 1$, increases very rapidly, which makes the computational cost of the problem unmanageable. In such cases, ANOVA decomposition can be used as an effective technique to significantly reduce the dimension of the random space [47].

Finally, we emphasize that SSPM provides a general and flexible framework, which naturally handles moving geometries [48]. This would make SSPM an efficient computational tool to study the effect of random roughness, e.g., in aerodynamic and turbo-machinery applications.

Acknowledgements

Appendix A. Random mapping approach

The mapping approach for solving PDEs on random domains consists of the following two steps. First, the random domain is mapped onto a deterministic domain. The random Jacobian trans-

formation renders a (deterministic or stochastic) governing PDE stochastic. Second, the transformed stochastic PDE in the deterministic domain is solved. This can be accomplished either analytically (e.g., via perturbation expansions [19]) or numerically (e.g., via either polynomial chaos [12] or stochastic collocation methods [13]). Here we use the generalized polynomial chaos (gPC) implementation of the approach described in [6]. It is briefly presented below for completeness.

A.1. Stochastic mapping onto a deterministic domain

Let us introduce a new coordinate system (η_1, η_2), in which the original stochastic flow domain $\mathcal{D} = \{(x_1, x_2) : 0 \leqslant x_1 \leqslant L_x, s(x_1; \omega) \leqslant x_2 \leqslant L_y\}$ takes the form of a deterministic rectangle $E = \{(\eta_1, \eta_2) : 0 \leqslant \eta_1 \leqslant L_x, 0 \leqslant \eta_2 \leqslant L_y\}$. A mapping $\mathcal{D} \rightarrow E$ is accomplished by a transformation of coordinates $\eta_i = \eta_i(x_1, x_2)$ $(i = 1, 2)$. For complex geometries, this stochastic mapping $\eta_i = \eta_i(x_1, x_2)$ and its inverse $x_i = x_i(\eta_1, \eta_2)$ are constructed [19,12,6] by solving Laplace's equations,

$$\frac{\partial^2 x_i}{\partial \eta_1^2} + \frac{\partial^2 x_i}{\partial \eta_2^2} = 0, \quad (\eta_1, \eta_2) \in E, \quad i = 1, 2. \tag{A.1}$$

subject to the boundary conditions

$$x_1(0, \eta_2) = 0, \quad x_1(L_x, \eta_2) = L_x, \quad x_1(\eta_1, 0) = \eta_1, \quad x_1(\eta_1, L_y) = \eta_1; \tag{A.2a}$$

$$x_2(0, \eta_2) = \eta_2, \quad x_2(L_x, \eta_2) = \eta_2, \quad x_2(\eta_1, 0) = s, \quad x_2(\eta_1, L_y) = L_y. \tag{A.2b}$$

Uncertainty (randomness) in domain geometry, $s(x_1, \omega)$, manifests itself in the mapping problem through a boundary condition in (A.2). The random field $s(x_1, \omega)$ is represented via a Karhunen–Loève expansion truncated after N terms. Solutions of (A.1), (A.2) can now be approximated by a series

$$x_i(\eta_1, \eta_2, \omega) = \sum_{k=0}^{N} \hat{x}_{i,k}(\eta_1, \eta_2) Y_k(\omega), \quad i = 1, 2. \tag{A.3}$$

Substituting (A.3) into (A.1) and taking a Galerkin projection yields $2(N + 1)$ Laplace's equations for the coefficients $\hat{x}_{i,k}(\eta_1, \eta_2)$,

$$\frac{\partial^2 \hat{x}_{i,k}}{\partial \eta_1^2} + \frac{\partial^2 \hat{x}_{i,k}}{\partial \eta_2^2} = 0, \quad (\eta_1, \eta_2) \in E, \quad i = 1, 2, \quad k = 0, \ldots, N. \tag{A.4}$$

The boundary conditions for (A.4) are derived by substituting (A.3) into (A.2) and taking a Galerkin projection. The resulting boundary-value problems are solved with a Chebyshev spectral method.

A.2. Transformed Stokes equations

The procedure outlined above enables one to compute a Jacobian transformation,

$$J(\eta_1, \eta_2, \omega) \equiv \frac{\partial(\eta_1, \eta_2)}{\partial(x_1, x_2)} = J[\eta_1, \eta_2, Y_1(\omega), \cdots, Y_N(\omega)] \tag{A.5}$$

and related transformation metrics

$$A = \frac{1}{J}\left[\left(\frac{\partial x_2}{\partial \eta_2}\right)^2 + \left(\frac{\partial x_1}{\partial \eta_2}\right)^2\right],$$

$$B = \frac{1}{J}\left(\frac{\partial x_2}{\partial \eta_1}\frac{\partial x_2}{\partial \eta_2} + \frac{\partial x_1}{\partial \eta_1}\frac{\partial x_1}{\partial \eta_2}\right),$$

$$C = \frac{1}{J}\left[\left(\frac{\partial x_2}{\partial \eta_1}\right)^2 + \left(\frac{\partial x_1}{\partial \eta_1}\right)^2\right]. \tag{A.6}$$

The flow Eqs. (9) are transformed into

$$\frac{\partial}{\partial \eta_1}\left(A\frac{\partial u_1}{\partial \eta_1} - B\frac{\partial u_1}{\partial \eta_2}\right) - \frac{\partial}{\partial \eta_2}\left(B\frac{\partial u_1}{\partial \eta_1} - C\frac{\partial u_1}{\partial \eta_2}\right)$$
$$= \frac{1}{\mu}\left(\frac{\partial x_2}{\partial \eta_2}\frac{\partial p}{\partial \eta_1} - \frac{\partial x_2}{\partial \eta_1}\frac{\partial p}{\partial \eta_2}\right), \tag{A.7a}$$

$$\frac{\partial}{\partial \eta_1}\left(A\frac{\partial u_2}{\partial \eta_1} - B\frac{\partial u_2}{\partial \eta_2}\right) - \frac{\partial}{\partial \eta_2}\left(B\frac{\partial u_2}{\partial \eta_1} - C\frac{\partial u_2}{\partial \eta_2}\right)$$
$$= \frac{1}{\mu}\left(\frac{\partial x_1}{\partial \eta_2}\frac{\partial p}{\partial \eta_2} - \frac{\partial x_1}{\partial \eta_2}\frac{\partial p}{\partial \eta_1}\right), \tag{A.7b}$$

$$\left(\frac{\partial x_2}{\partial \eta_2}\frac{\partial u_1}{\partial \eta_1} - \frac{\partial x_2}{\partial \eta_1}\frac{\partial u_1}{\partial \eta_2}\right) - \left(\frac{\partial x_1}{\partial \eta_2}\frac{\partial u_2}{\partial \eta_1} - \frac{\partial x_1}{\partial \eta_1}\frac{\partial u_2}{\partial \eta_2}\right) = 0. \tag{A.7c}$$

A.3. Solution of stochastic flow equations

Let $\{\Psi_m(\mathbf{Y})\}_{m=0}^{M}$ denote a set of multidimensional orthogonal polynomials of the random vector $\mathbf{Y}(\omega) \equiv (Y_1, \ldots, Y_N)^T$ of the N independent random variables $Y_1(\omega), \ldots, Y_N(\omega)$ introduced in (A.3). The polynomials are chosen to have the ensemble means $\overline{\Psi}_0 = 1$ and $\overline{\Psi}_k = 0$ $(k \geqslant 1)$ and satisfy the orthogonality condition

$$\overline{\Psi_i \Psi_j} = \overline{\Psi_i^2}\delta_{ij}, \quad \overline{\Psi_i \Psi_j} \equiv \int \Psi_i(\mathbf{Y})\Psi_j(\mathbf{Y})W(\mathbf{Y})\mathrm{d}Y_1 \ldots \mathrm{d}Y_N, \tag{A.8}$$

where $W(\mathbf{Y})$ is a weight function corresponding to a given polynomial type.

The size of the polynomial set, M, is determined by the "stochastic dimension" N and the order P of polynomials Ψ_k, according to

$$M = \frac{(N + P)!}{N!P!} - 1. \tag{A.9}$$

Polynomial chaos expansions (PCEs) represent a system state, e.g., pressure $p(\boldsymbol{\eta}, \omega)$, a random field whose ensemble statistics are to be determined, as a series

$$p(\eta, \omega) = \sum_{k=0}^{M} \hat{p}_k(\eta)\Psi_k[\mathbf{Y}(\omega)]. \tag{A.10}$$

Similar expansions are employed for the other two state variables, $u_1(\eta, \omega)$ and $u_2(\eta, \omega)$ and metrics coefficients, $A(\eta, \omega), B(\eta, \omega)$ and $C(\eta, \omega)$. Substituting these expansions into (A.7) and taking a Galerkin projection, one obtains a set of deterministic equations for the coefficients $\{\hat{p}_k(\eta)\}_{k=0}^{M}, \{\hat{u}_k(\eta)\}_{k=0}^{M}$ and $\{\hat{v}_k(\eta)\}_{k=0}^{M}$. These equations were solved using a spectral element method.

References

[1] K.S. Deffeyes, B.D. Ripley, G.S. Watson, Stochastic geometry in petroleum geology, Math. Geol. 14–5 (1982) 419–432.

[2] L.W. Mays, Water Distribution Handbook, McGrow-Hill, 1999.

[3] M. Miller, A. Cerezo, M. Hetherington, G. Smith, Atom Probe Field Ion Microscopy, Monographs on the Physical and Chemistry of Materials, Oxford University Press, Oxford, UK, 1996.

[4] A. Bejan, Shape and Structure, from Engineering to Nature, Cambridge University Press, 2000.

[5] M. Nosonovsky, B. Bhushan, Biologically inspired surfaces: broadening the scope of roughness, Adv. Funct. Mater. 18 (2008) 843–855.

[6] S.-W. Park, M. Intaglietta, D.M. Tartakovsky, Impact of endothelium roughness on blood flow, J. Theor. Biol. 300 (2012) 152–160.

[7] G. Taylor, A model for the boundary condition of a porous material: Part I, J. Fluid Mech. 49 (1971) 319–326.

[8] S. Richardson, A model for the boundary condition of a porous material: Part II, J. Fluid Mech. 49 (1971) 327–336.

[9] M. Fyrillas, C. Pozrikidis, Conductive heat transport across rough surfaces and interfaces between two conforming media, Int. J. Heat Mass Transfer 49 (2001) 1789–1801.

[10] K. Sarkar, C. Meneveau, Gradients of potential fields on rough surfaces: perturbative calculation of the singularity distribution function $f(\alpha)$ for small surface dimension, Phys. Rev. E 47 (1993) 957–966.

[11] J. Rudzitis, V. Padamans, E. Bordo, R. Haytham, Random process model of rough surfaces contact, Meas. Sci. Technol. 9 (7) (1998) 1093–1097.
[12] D. Xiu, D.M. Tartakovsky, Numerical methods for differential equations in random domains, SIAM J. Sci. Comput. 28 (3) (2006) 1167–1185.
[13] D.M. Tartakovsky, D. Xiu, Stochastic analysis of transport in tubes with rough walls, J. Comput. Phys. 217 (1) (2006) 248–259.
[14] D. Cajueiro, V. Sampaio, C. de Castilho, R. Andrade, Fractal properties of equipotentials close to a rough conducting surface, J. Phys. Condens. Matter 11 (1999) 4985–4992.
[15] I. Babuska, J. Chleboun, Effects of uncertainties in the domain on the solution of Neumann boundary value problems in two spatial dimensions, Math. Comput. 71 (2002) 1339–1370.
[16] I. Babuska, J. Chleboun, Effects of uncertainties in the domain on the solution of Dirichlet boundary value problems, Numer. Math. 93 (2003) 583–610.
[17] L. Parussini, V. Pediroda, C. Poloni, Prediction of geometric uncertainty effects on fluid dynamics by polynomial chaos and fictitious domain method, Comput. Fluids 39 (1) (2010) 137–151.
[18] L. Mathelin, M.Y. Hussaini, T.A. Zang, Stochastic approaches to uncertainty quantification in CFD simulations, Numer. Algorithms 38 (1–3) (2005) 209–236.
[19] Y.N. Lazarev, P.V. Petrov, D.M. Tartakovsky, Interface dynamics in randomly heterogeneous porous media, Adv. Water Resour. 28 (4) (2005) 393–403.
[20] P. Tsuji, D. Xiu, L. Ying, A fast method for high-frequency acoustic scattering from random scatterers, Int. J. Uncert. Quant. 1–99 (2011) 99–117.
[21] Y. Nakayama, R. Yamamoto, Simulation method to resolve hydrodynamic interactions in colloidal dispersions, Phys. Rev. E 71 (2005) 036707–036713.
[22] K. Kim, Y. Nakayama, R. Yamamoto, A smoothed profile method for simulating charged colloidal dispersions, Comput. Phys. Commun. 169 (2005) 104–106.
[23] R. Yamamoto, Y. Nakayama, K. Kim, A method to resolve hydrodynamic interactions in colloidal dispersions, Comput. Phys. Commun. 169 (1–3) (2005) 301–304.
[24] Y. Nakayama, K. Kim, R. Yamamoto, Hydrodynamic effects in colloidal dispersions studied by a new efficient direct simulation, in: Flow Dynamics, vol. 832 of Am. Inst. Phys. Conf. Ser., 2006, pp. 245–250.
[25] Y. Nakayama, K. Kim, R. Yamamoto, Simulating (electro) hydrodynamic effects in colloidal dispersions: smoothed profile method, Eur. Phys. J. E 26 (4) (2008) 361–368.
[26] K. Kim, Y. Nakayama, R. Yamamoto, Direct numerical simulations of electrophoresis of charged colloids, Phys. Rev. Lett. 96 (20) (2006) 208–302.
[27] R. Yamamoto, K. Kim, Y. Nakayama, Strict simulations of non-equilibrium dynamics of colloids, Colloids Surf. A 311 (1–3) (2007) 42–47.
[28] X. Luo, M.R. Maxey, G.E. Karniadakis, Smoothed profile method for particulate flows: error analysis and simulations, J. Comput. Phys. 228 (2009) 1750–1769.
[29] J.A. Sethian, A fast marching level set method for monotonically advancing fronts, Proc. Natl. Acad. Sci (1995) 1591–1595.

[30] C.H. Su, D. Lucor, Covariance kernel representations of multidimensional second-order stochastic processes, J. Comput. Phys. 217 (1) (2006) 82–99.
[31] I. Babuska, F. Nobile, R. Tempone, A stochastic collocation method for elliptic partial differential equations with random input data, SIAM J. Numer. Anal. 45 (3) (2007) 1005–1034.
[32] G.E. Karniadakis, M. Israeli, S.A. Orszag, High-order splitting methods for the incompressible Navier–Stokes equations, J. Comput. Phys. 97 (1991) 414.
[33] G.E. Karniadakis, S.J. Sherwin, Spectral/hp Element Methods for CFD, second ed., Oxford University Press, New York, 2005.
[34] D. Funaro, D. Gottlieb, A new method of imposing boundary conditions in pseudospectral approximations of hyperbolic equations, Math. Comput. 51 (184) (1988) 599–613.
[35] J.S. Hesthaven, D. Gottlieb, A stable penalty method for the compressible Navier–Stokes equations: I. Open boundary conditions, SIAM J. Sci. Comput. 17 (3) (1996) 579.
[36] J. Foo, X. Wan, G.E. Karniadakis, The multi-element probabilistic collocation method (ME-PCM): error analysis and applications, J. Comput. Phys. 227 (2008) 9572–9595.
[37] B. Oksendal, Stochastic Differential Equations, Springer-Verlag, 1998.
[38] S. Smolyak, Quadrature and interpolation formulas for tensor products of certain classes of functions, Soviet Math. Dokl. 4 (1963) 240–243.
[39] S. Pope, Turbulent Flows, Cambridge University Press, New York, NY, 2000.
[40] E. Achenbach, E. Heinecke, On vortex shedding from smooth and rough cylinders in the range of Reynolds numbers 6×10^3 to 5×10^6, J. Fluid Mech. 109 (1981) 239–251.
[41] X. Wan, Adaptive multi-element generalized polynomial chaos: algorithms and applications, Ph.D. thesis, Brown University, 2007.
[42] X. Wan, G. Karniadakis, Long-term behavior of polynomial chaos in stochastic flow simulations, Comput. Methods Appl. Mech. Engrg. 195 (2006) 5582–5596.
[43] E. Novak, K. Ritter, High dimensional integration of smooth functions over cubes, Numer. Math. 163 (2000) 51–59.
[44] E. Novak, K. Ritter, Simple cubature formulas with high polynomial exactness, Constr. Approx. 15 (1999) 499–522.
[45] V. Barthelmann, E. Novak, K. Ritter, High dimensional polynomial interpolation on sparse grids, Adv. Comput. Math. 12 (2000) 273–288.
[46] D.M. Tartakovsky, C.L. Winter, Dynamics of free surfaces in random porous media, SIAM J. Appl. Math. 61 (6) (2001) 1857–1876.
[47] X. Yang, M. Choi, G. Lin, G.E. Karniadakis, Adaptive ANOVA decomposition of stochastic incompressible and compressible flows, J. Comput. Phys. 231 (2012) 1587–1614.
[48] X. Luo, C. Chryssostomidis, G.E. Karniadakis, Spectral element/smoothed profile method for turbulent flow simulations of waterjet propulsion systems, in: Proceedings of Grand Challenges in Modeling Simulation, Summer Simulation Multiconference, July 2010, Ottawa, Canada.